VTT Technical Research Centre of Finland

Localised electrochemical processes on laser powder bed fused 316 stainless steel with various heat treatments in high-temperature water

Que, Zaiqing; Chang, Litao; Saario, Timo; Bojinov, Martin

Link to publication

Check for updates

Localised electrochemical processes on laser powder bed fused 316 stainless steel with various heat treatments in high-temperature water

Zaiqing Que [a],[*], Litao Chang [b],[c],[**], Timo Saario [a], Martin Bojinov [d]

[a] *Advanced Materials for Nuclear Energy, VTT Technical Research Centre of Finland, Espoo, Finland*
[b] *Shanghai Institute of Applied Physics, Chinese Academy of Sciences, Shanghai, China*
[c] *University of Chinese Academy of Sciences, Beijing, 100049, China*
[d] *Department of Physical Chemistry, University of Chemical Technology and Metallurgy, Sofia, Bulgaria*

A B S T R A C T

Laser powder bed fusion (LPBF) is an advanced additive manufacturing technology for stainless steel components fabrication, and a comprehensive understanding of electrochemical behaviour of the LPBF stainless steels is critical for expanding their applications in nuclear and other high-temperature water environments. In the present study, comparison of microstructure and high-temperature electrochemical behaviours between LPBF 316 and wrought 316 in simulated pressurized water reactor environment was made. Three heat treatments, stress relieving (SR), solution annealing (SA) and hot isostatic pressing (HIP), were used to heat treat the LPBF 316. The results showed that both the yield strength and impact energy of the SA and HIP treated LPBF 316 were lower than that of the SR treated sample, whilst the tensile elongation of the SA and HIP treated samples was higher than SR treated sample. These changes were found to be due to the disappearance of the cellular structures, decrease in the dislocation density and the occurrence of recrystallization during the treatments. Electrochemical impedance spectroscopy measurements at 288 °C and their interpretation with the Mixed-Conduction Model indicated that corrosion rate of the heat-treated LPBF 316 variants is significantly lower than that of the wrought 316. In addition, SR material exhibits marginally lower corrosion rates than SA and HIP ones. Microstructure examination after high-temperature water exposure revealed an inhomogeneous inner oxide layer on LPBF 316 in contrast to the thicker and more uniform inner oxide layer on wrought 316. The localised nature of electrochemical processes is suggested to be induced by the nano-precipitates in the LPBF samples.

1. Introduction

Additive manufacturing (AM), or 3D printing, is a type of novel and continuously expanding technology due to its ability to produce components with complex geometry that requires limited amount of final finishing, reduce the lead-time and material waste and minimise carbon footprint [1,2]. AM techniques have been proven to be beneficial in numerous industries such as aerospace, defence, medical, automobile and recently, nuclear [3]. The AM fuel assembly bracket installed in the Browns Ferry nuclear power plant in spring 2021 is the first safety-related 3D-printed component in a commercial reactor [4,5]. Laser powder bed fusion (LPBF) is the most widely used AM technique for various materials [6–9], it has also been listed as one of the most promising manufacturing technique for nuclear components. Type 316 stainless steel is one of the most widely used materials in nuclear power plants, and it is usually produced *via* cast and wrought routes. Compared to cast or wrought 316, as-deposited LPBF 316 exhibits much higher strength and hardness [10,11], although its ductility could be slightly lower than that of the wrought counterpart in certain conditions [12,13]. The unique mechanical properties for the LPBF 316 are mainly due to the formation of non-equilibrium melt pools and a rigid hierarchical or gradient heterogeneous microstructure during the rapid melting and solidification [1,10,14–16]. However, microstructure and mechanical properties of the AM materials are always anisotropic because of textures developed during the building process [17], which is a key issue for components that will bear multiaxial loads during service.

---

* Corresponding author.
** Corresponding author at: Shanghai Institute of Applied Physics, Chinese Academy of Sciences, Shanghai, China.
E-mail addresses: zaiqing.que@vtt.fi (Z. Que), changlitao@sinap.ac.cn (L. Chang).

Heat treatments have been widely used to optimize the microstructure of AM parts to obtain dynamic mechanical properties (*e.g.* toughness and fatigue resistance) comparable to traditionally produced components [17]. Typical procedures include low-temperature heat treatments to relieve residual stresses (*e.g.* stress relieving (SR) treatment), and high-temperature heat treatments (*e.g.* solution annealing (SA) and hot isostatic pressing (HIP)) that aim at inducing recovery and recrystallization to reduce the anisotropy in microstructure and mechanical properties. SR and SA are easy-to-conduct processes, however, they may not induce dramatic change in microstructure, and also cannot close the pores in the LPBF materials, such as 316. Hierarchical microstructure can always exist in the AM 316 after SR and SA treatments, which lead to anisotropy in both corrosion and cracking behaviours [18]. In addition to high temperature, high pressure can also be applied to the materials during HIP. Therefore, HIP has been suggested as a superior post-AM heat treatment for materials/components to be used in nuclear high-temperature water environments by ensuring equiaxed microstructure and minimizing the porosity [19,20].

The general effects of post treatments on microstructure, mechanical and room-temperature corrosion properties of AM stainless steels are thought to be understood. However, discrepancies in literature data still exist [21–23]. For example, results by Kong et al. [24] show that anisotropy in microstructure and mechanical properties for AM 316 can be eliminated *via* a 1200 °C/2 h heat treatment, which can induce complete recrystallization. However, other researchers did not observe complete recrystallization after heat treatments with similar parameter [13,25]. Further, Ettefagh et al. [26] reported that post-AM treatment at temperatures > 1000 °C promotes diffusion and formation of inclusions, which reduces corrosion resistance. Similarly, Laleh et al. [27,28] reported that even if as-deposited LPBF 316 has a significantly higher pitting resistance than the commercial counterpart, subsequent post-AM treatment at T > 1000 °C drastically reduces it due to changes in morphology and chemistry of inclusions. In contrast, Dong et al. [29] reported that after a 750 °C/2 h heat treatment, the SCC susceptibility of LPBF 316 was reduced. To date, it is not yet fully understood how post-AM heat treatments influence the corrosion response of LPBF 316. Moreover, most corrosion or electrochemical studies on AM materials were performed in the low-temperature range (< 100 °C).

To the best of the authors' knowledge, studies on the corrosion behaviour of AM 316 in high-temperature water environments for nuclear applications (> 280 °C) are very limited, and no work has been done to date to address high-temperature electrochemical behaviour after heat treatments. A comprehensive understanding of high-temperature electrochemical behaviour of AM stainless steels is critical for their applications in nuclear and other harsh environments. In view of this, high-temperature electrochemical properties, microstructure evolution and mechanical characteristics of various post-LPBF heat-treated 316 have been investigated in the present study. Detailed analytical electron microscopy characterisations and mechanical tests were carried out on LPBF 316 subjected to three heat treatment procedures using nuclear-grade (NG) wrought 316 as reference. High-temperature electrochemical impedance spectroscopic (EIS) measurements were conducted to evaluate corrosion rates as depending on heat treatment. After exposure, specimens were characterised with scanning electron microscopy (SEM) and glow discharge optical emission spectrometry (GDOES) to estimate the composition and structure of the oxide films. EIS interpretation with the Mixed-Conduction Model (MCM) was performed to estimate the rate constants of charge transfer processes at the metal/film (M/F) and film/solution (F/S) interfaces, as well as diffusion coefficients through the passive layer that determine the corrosion behaviour of the investigated materials.

2. Experimental

2.1. Material, LPBF process and heat treatments

Nitrogen gas atomized 316 powder with an average particle size of 36 μm was used for LPBF. The chemical composition of the powder is shown in Table 1. The specimens were prepared using an EOS M 290 machine under industrial-grade Ar environment in the build chamber. The printing layer thickness was 20 μm at a platform set temperature of 80 °C using a ceramic re-coater blade. The laser parameters were adopted from the 316L_SurfaceM291 1.10 parameter set [13]. Specimens were deposited directly on the build platform in a vertical orientation without an additional support structure. The post treatments employed were SR, SA and HIP. The SA and HIP treatments were performed on the SR treated bars. The SR scheme was selected according to the stress reliving scheme for stainless steel weldment; the SA scheme was the annealing scheme which can induced complete recrystallization in wrought stainless steels; the HIP scheme, 1150 °C/100 MPa/4 hr, was the scheme usually used to consolidate stainless steel powder, for powder-metallurgy HIP processing. Details of the heat treatments are given in Table 2.

Wrought 316 was fabricated by Creusot-Loire Industrie from castings and qualified to be used for tubes in the nuclear sector. The fabrication process, chemical composition, microstructure and mechanical properties of this NG reference material comply with the RCC-M M3307 level 3 specification. Its chemical composition is also shown in Table 1. The chemical compositions of both LPBF powder and wrought 316 fulfil the requirements of procurement guideline for NG 316 stainless steel [30].

2.2. Mechanical tests

Specimens for tensile and V-notch impact toughness tests were machined from the heat-treated round bars along the build direction. Tensile tests (cylindrical specimens with a diameter of 5 mm) were performed according to ISO-6892 method with a strain rate of 0.00025 s^{-1} at room temperature. Five tensile tests were performed for each condition.

The V-notch impact toughness tests (Charpy specimen with size of $10 \times 10 \times 55$ mm) were conducted according to ISO 148–1:2016 using a Losenhausenwerk-MFL 1959 with 300 J impact pendulum at room temperature. Four tests were performed for each condition at room temperature. The specimens for microstructure characterisation were machined and prepared from Charpy specimens, having impact energies close to the average values measured in the program.

2.3. Electrochemical tests

Specimens for EIS measurements were cut from the non-deformed regions of the Charpy specimens with a blade saw along the building direction. The NG wrought 316 sample was prepared along the longitudinal direction on the LS plane. Specimens ($1 \times 1 \times 0.3$ cm) with 0.25 μm final finish (after grinding progressively using grinding papers and polished with 3 μm and 1 μm diamond paste) were used in the high-temperature electrochemical tests. A Ni measurement wire was spot welded onto the side of the specimens.

The high-temperature electrochemical measurements were performed in an AISI 316 L stainless steel autoclave connected to a recirculating loop. Three post-LPBF heat-treated specimens and one wrought 316 specimen were exposed to high-temperature water for 160 h in the autoclave. The high-temperature water environment applied was the pressurized water reactor (PWR) beginning of cycle water chemistry, *i.e.* 2.2 ppm Li (as LiOH), 1000 ppm B (5700 ppm of H_3BO_3) and 35 cm^3 H_2 / kg H_2O, with a pH of 7.0 at 288 °C. A pH-electrode with Ni/NiO couple was used as reference electrode. EIS measurements were performed after *ca.* 50 and 100 h of exposure with a CompactStat potentiostat (Ivium) at the open-circuit potential (E_{oc}) in the frequency range from 100 kHz to

Table 1

Chemical composition (wt%) of the applied 316 AM powder and NG wrought 316 material.

	Fe	Cr	Ni	Mo	Mn	Si	N	Cu	C	S	P
316 powder	Bal.	17.9	14.0	2.7	1.5	0.25	0.07	< 0.01	0.005	0.005	< 0.01
Wrought 316	Bal.	17.3	11.5	2.6	1.8	0.37	0.05	0.024	0.027	0.004	0.03

Table 2

Summary of the post-LPBF heat treatments investigated in this work.
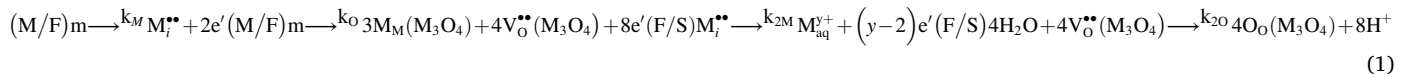
Heat treatment	Parameters
SR	Hold at 650 °C for 2 h (argon atmosphere) and cool in air
SA	SR+ annealed at 1066 °C for 1 h in argon atmosphere followed by air cooling as per AMS 2759 standard
HIP	SR+ HIP at 1150 °C for 4 h in 100 MPa argon atmosphere and furnace cooled

0.1 mHz using an ac amplitude of 50 mV (rms). The E_{oc} was *ca.* −0.77 V_{SHE} for all the specimens.

2.4. Electrochemical modelling

The EIS data were quantitatively interpreted with the MCM [31,32] to estimate the kinetic and transport parameters of oxide film formation and corrosion release of the investigated materials.

According to the model, if both oxide layer formation/dissolution and dissolution of metals through the oxide ("corrosion release") are taken into consideration for a spinel-type oxide film (M_3O_4), the following reactions occur at the interfaces:
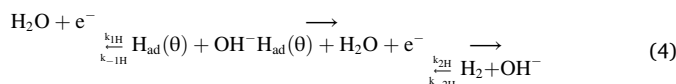
$$(M/F)m \xrightarrow{k_M} M_i^{\bullet\bullet} + 2e' \, (M/F)m \xrightarrow{k_O} 3M_M(M_3O_4) + 4V_O^{\bullet\bullet}(M_3O_4) + 8e' \, (F/S)M_i^{\bullet\bullet} \xrightarrow{k_{2M}} M_{aq}^{y+} + \left(y-2\right)e' \, (F/S)4H_2O + 4V_O^{\bullet\bullet}(M_3O_4) \xrightarrow{k_{2O}} 4O_O(M_3O_4) + 8H^+ \tag{1}$$

where m is an atom (Fe, Cr, Ni) in the alloy, and the other symbols are consistent with a Kroger-Vink notation (M_M and O_O are normal cation and oxygen positions, $M_i^{\bullet\bullet}$ is an interstitial cation, $V_O^{\bullet\bullet}$ an oxygen vacancy, and M_{aq}^{y+} a cation in the solution). Formation of metal hydroxides is neglected in the present treatment since we are considering the system in a quasi-steady state, and the hydroxides that are formed in the initial stages of the metal/water interaction are transformed into spinel oxides *via* reactions of the type

$$3M(OH)_2 \rightarrow M_3O_4 + H_2O + 2H^+ + 2e' \tag{2}$$
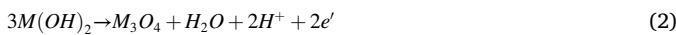
The interfacial steps are coupled *via* transport of oxygen vacancies and interstitial cations through the barrier part of the oxide, assumed to be governed by diffusion and migration. Consequently, the transfer function to describe the impedance spectra is as follows:

$$Z = R_{el} + Z_{F/S} + Z_f \tag{3}$$

The process at the F/S interface is most probably dominated by the water reduction-hydrogen oxidation reaction that is assumed to obey a Volmer-Heyrovsky mechanism:

$$H_2O + e^- \underset{k_{-1H}}{\overset{k_{1H}}{\rightleftharpoons}} H_{ad}(\theta) + OH^- \, H_{ad}(\theta) + H_2O + e^- \underset{k_{-2H}}{\overset{k_{2H}}{\rightleftharpoons}} H_2 + OH^- \tag{4}$$

where θ is the surface coverage with atomic hydrogen (H_{ad}). The charge balance (current density) at the F/S interface is written as:

$$I = F(k_{-2H}c_{H_2} - k_{1H} + (y-2)k_{2M})(1-\theta) + (k_{-1H} - k_{2H})\theta \tag{5}$$

As the last reaction in Eq. (1) does not involve charge transfer, it does not participate in the balance.

Assuming a Langmuir-type isotherm for the adsorbed H, the material balance for the surface coverage θ with adsorbed intermediate is given by the expression:

$$\beta \frac{d\theta}{dt} = (k_{-2H}c_{H_2} + k_{1H})(1-\theta) - (k_{-1H} + k_{2H})\theta \tag{6}$$

where β is the concentration of active sites for adsorption in mol·cm^{-2} and c_{H_2} the concentration of dissolved hydrogen in mol·cm^{-3}. Assuming that the rate constants of the respective steps depend exponentially on applied potential:

$$k_i = k_i^0 \exp(\pm b_i E), b_i = \alpha_i \frac{F}{RT}, i = 1H, -1H, 2H, -2H, 2M, 2O \tag{7}$$

the impedance of the F/S interface is obtained as a small amplitude ac solution of Eqs. (5)–(6):

$$Z_{F/S} = \frac{1}{R_{F/S}^{-1} + \frac{AX}{Z+j\omega\beta} + j\omega C_{F/S}} \tag{8}$$

The relationships between parameters $R_{F/S}$, A, X, Z and the reaction rate constants are given by the expressions:

$$R_{F/S}^{-1} = F(k_{-1H}b_{-1H} + k_{2H}b_{2H})\overline{\theta} + F(k_{2H}b_{2H}c_{H_2} + k_{1H}b_{1H} + (y-2)k_{2M}b_{2M})(1-\overline{\theta})$$

$$A = F(k_{1H} + k_{-1H} - k_{-2H}c_{H_2} - k_{2M} - k_2)$$

$$X = k_{-2H}b_{-2H}c_{H_2} - (k_{-2H}b_{-2H}c_{H_2} - k_{1H}b_{1H} + k_{-1H}b_{-1H} - k_{2H}b_{2H})\overline{\theta} - k_{1H}b_{1H}$$

$$\overline{\theta} = \frac{k_{2H}c_{H_2} + k_{1H}}{Z}, Z = k_{-2H}c_{H_2} + k_{1H} + k_{-1H} + k_{2H} \tag{9}$$

Moreover, the impedance of the oxide film is represented as a parallel combination of the impedance of its electronic properties, Z_e, and two ionic transport impedances pertinent to the oxygen vacancies ($Z_{ion,O}$) and interstitial cations ($Z_{ion,M}$), respectively:

$$Z_f = \left(Z_e^{-1} + Z_{ion,O}^{-1} + +Z_{ion,M}^{-1}\right)^{-1} \tag{10}$$

The explicit expressions for these impedances are given as:

$$Z_e \approx \frac{RT}{2j\omega F \overrightarrow{E} LC_{sc}} \ln \frac{[1 + j\omega\rho_d\varepsilon\varepsilon_0 \exp(2KL)]}{1 + j\omega\rho_d\varepsilon\varepsilon_0}, K = \frac{F}{RT}\overrightarrow{E}, \rho_d$$

$$= \frac{RT}{F^2 D_e} \frac{k_{2O} + k_{2M}}{k_O + k_M} \tag{11}$$

$$Z_{ion,O} \approx \frac{RT}{4F^2 k_O \left(1-\alpha\right)\left(1+\sqrt{1+\frac{4j\omega}{D_O K^2}}\right)}, Z_{ion,M}$$

$$\approx \frac{RT}{4F^2 k_M \left(1-\alpha\right)\left(1+\sqrt{1+\frac{4j\omega}{D_M K^2}}\right)} \qquad (12)$$

where D_e, D_O and D_M are the diffusion coefficients of electronic carriers, oxygen vacancies and interstitial cations, L the thickness of the barrier part of the oxide layer, $\vec{E}$ the field strength in that barrier part, ε the dielectric constant and α the potential consumer in the barrier part at the F/S interface. Finally, the total impedance is written as

$$Z = R_{el} + \left(Z_e^{-1} + Z_{ion,O}^{-1} + Z_{ion,M}^{-1}\right)^{-1} + Z_{F/S} \qquad (13)$$

The fitting of the experimental data to the MCM equations is performed using complex non-linear least squares method *via* user functions implemented in Originlab software. Statistical weighting is used for the data sets and the errors of estimate are multiplied by the reduced value of χ^2 resulting from the regression. Parameters that exhibited a mutual dependence larger than 0.67 were not fitted simultaneously in order to obtain statistically valid values of all considered parameters.

2.5. Microstructure characterisation

Microstructural characterisation of the samples, including the powder particles, post-AM heat-treated samples and samples after high-temperature water exposure, was performed using an optical microscopy, a Zeiss Crossbeam 540 SEM with solid-state four-quadrant backscatter detector and EDAX Hikari Plus electron backscatter diffraction (EBSD) detector, a Zeiss Merlin Compact SEM equipped with Oxford Instrument EBSD detector, an FEI TECNAI F20 field emission gun transmission electron microscope (TEM) and a Thermal Fisher Talos F200X analytical TEM with Super-X (4 SDDs) operated at 200 kV.

Secondary electron (SE) imaging was used for morphology observations, whilst back-scattered electron (BSE) imaging was performed for Z-contrast and grain orientation (using electron channelling contrast) observation. Porosity in the samples was measured from the optical microscopy images taken on the as-polished samples, the pores covered ~0.3% of the area in the SR and SA samples, whilst only tiny spherical pores were rarely observed in the HIP sample, and the coverage was near zero. The appearance of the pores was similar to that reported by other researchers [33] and was not shown in this paper for brevity. Cross-sectional samples were mounted in conductive resin and polished down to mirror surface finish using oxide suspension. The parameters for SE and BSE imaging were: 5 KeV, 0.5 nA with a working distance (WD) of 6–7 mm and 15 KeV, 1.5 nA with a WD of 5–7 mm, respectively. The WD for EBSD analysis was selected at 12–15 mm with samples tilted and the scanning step size was 50 nm. The mapping area was 700 μm in width and 700 μm in height for all samples, and only a portion of the map was shown in the paper to highlight the features in the material. EBSD inversed pole figure (IPF), phase map, kernel average misorientation (KAM) map and geometrically necessary dislocation (GND) map were analysed. Oxide layers were analysed with SEM-Energy Dispersive X-Ray (EDX). Samples for TEM characterisation were prepared through grinding thin foils down to 60–80 μm, and then electro-polishing using a double jet Struers Tenupol 5 equipped with a Jubalo closed-cycle system. The electrolyte used was 10% $HClO_4$ in acetic acid at room temperature. The scanning duration for STEM-EDX was 30 min for each sample using the Super-X Silicon Drift detectors of the Talos TEM, which was sufficient to reveal the element distribution variation.

GDOES elemental depth profile analysis was performed after high-temperature water exposure at two locations on each specimen. The GDOES spectrometer has been calibrated using certified reference materials. Measurements were performed according to ISO14707, ISO25138:2010 and ISO/DIS16962.2, whenever those were applicable.

Table 3
Summary of mechanical properties with different post-LPBF heat treatments in comparison to the wrought 316 material.

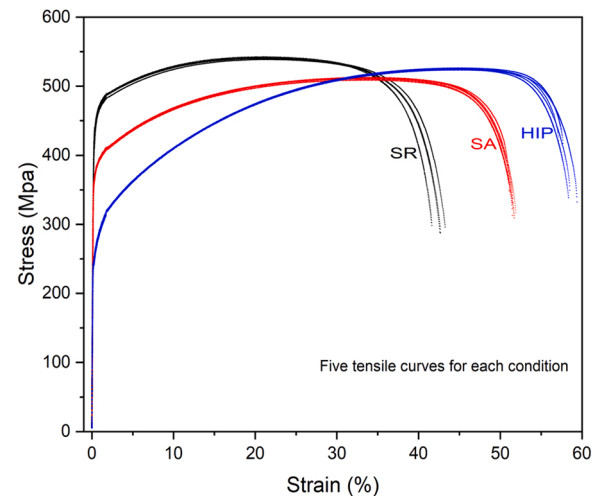| Heat treatments	Impact toughness testing	Tensile testing		
	Impact energy (J)	Yield strength (MPa)	Tensile strength (MPa)	Elongation (%)
SR	194 ± 4	430 ± 2	570 ± 4	45 ± 2
SA	161 ± 3	365 ± 4	542 ± 2	53 ± 1
HIP	154 ± 2	252 ± 2	552 ± 3	57 ± 2
NG wrought 316	120 ± 2	231 ± 1	554 ± 2	62 ± 2

Fig. 1. Tensile stress-strain curves for SR, SA and HIP heat-treated LPBF samples.

Depth profile analyses of oxidised steel samples were performed in the pressure-regulated mode applying a constant voltage of 800 V and a pressure of 3 hPa in pulse mode (pulse frequency of 2223 Hz, duty cycle of 20% and on-time of 90 μs). The diameter of the anode was 2.5 mm.

3. Results

3.1. Mechanical properties

A summary of the mechanical properties of post-LPBF heat-treated specimens and the NG wrought 316 specimen is presented in Table 3. The tensile stress-strain curves for SR, SA and HIP heat-treated LPBF 316 samples are shown in Fig. 1. Samples that received SR and HIP heat treatments exhibit the highest and lowest impact energy among the three heat treatment conditions, respectively. The yield strength for samples follows the same tendency as impact toughness. However, the ultimate tensile strength and fracture elongation ratio of the HIP sample were only marginally lower and higher than those of the SA sample.

Yield strength and impact toughness of the HIP sample are higher than those of wrought 316. The ultimate tensile strength and fracture elongation ratio of HIP sample are identical to those of the wrought material within the scatter range. According to the procurement guideline of NG 316 stainless steel [30], the mechanical properties of all four conditions are acceptable for application in nuclear field.

3.2. Microstructural characterisations

3.2.1. Wrought 316 microstructure

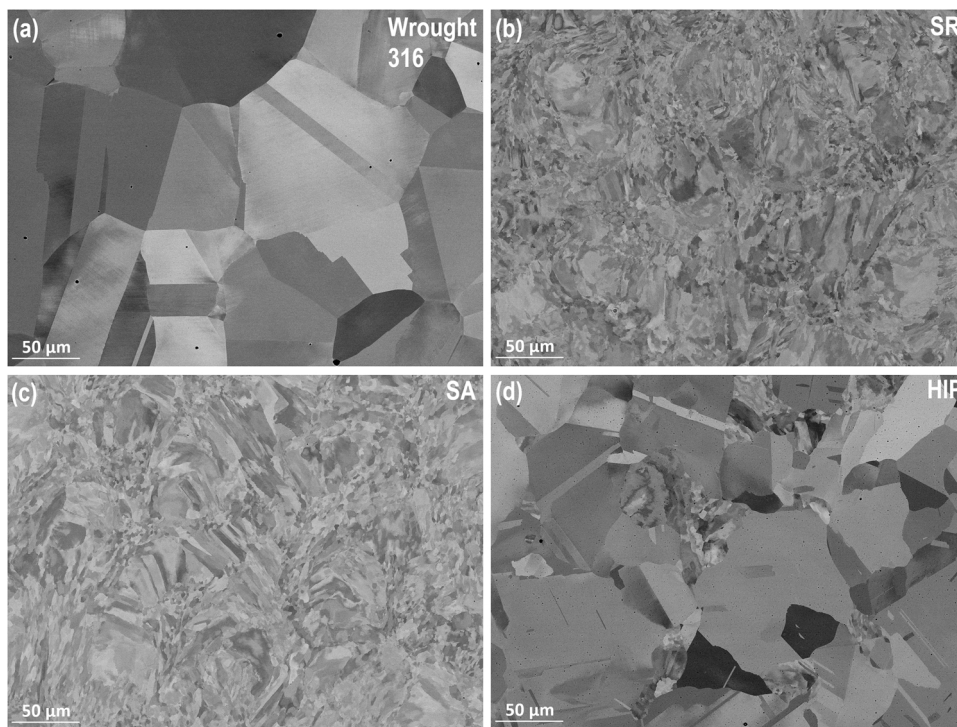The wrought 316 material that was processed through the cast &

Fig. 2. (a-b) SEM-BSE images of (a) wrought 316, (b) SR, (c) SA and (d) HIP heat-treated LPBF samples. The building direction is along the vertical direction of the images for (b-d).
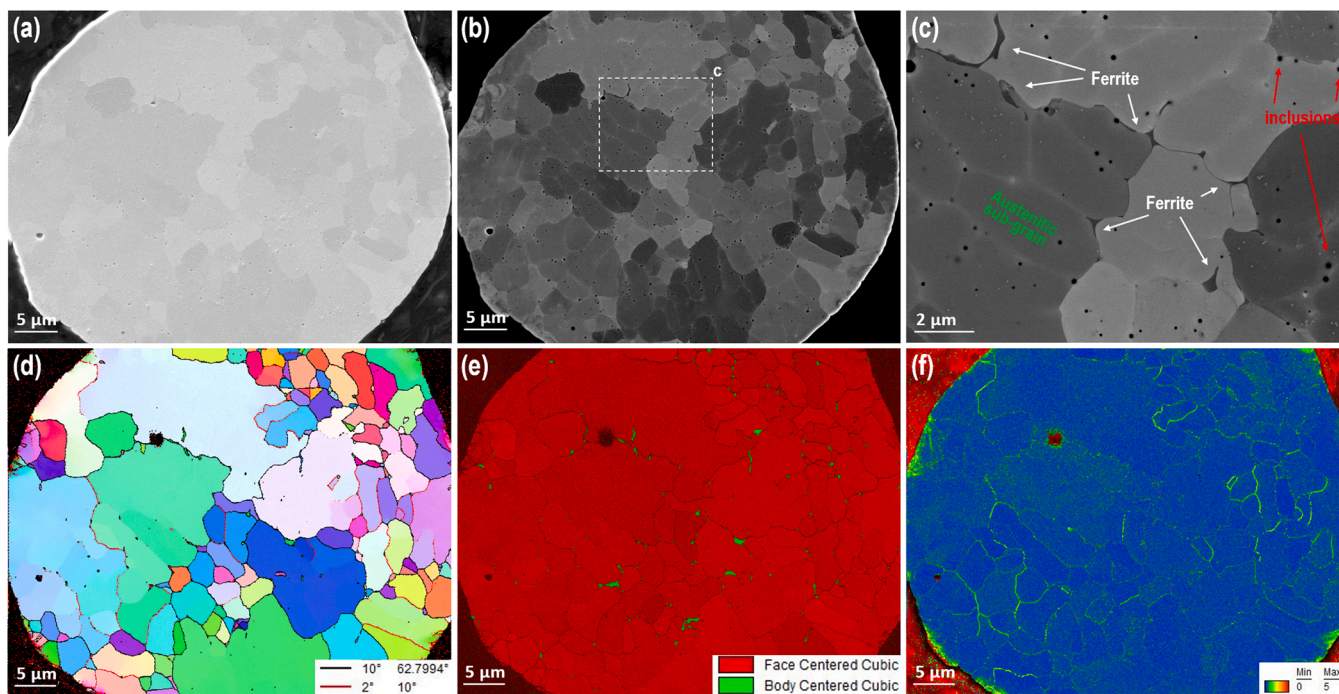

Fig. 3. 316 powder characterisation. (a) SEM-SE image; (b-c) SEM-BSE images; (d) EBSD IPF with rotation angle; (e) EBSD phase map; (f) EBSD KAM map.

wrought route has a fully recrystallized microstructure with equiaxed austenitic grains of ~120 μm. The most common inclusions in the wrought 316 material are (O, Al, Ti)-enriched oxides containing Cr and Mn and MnS containing traces of Cu and Ca. The average diameter of inclusions is roughly 2–6 μm. Randomly-distributed isolated dislocations were found throughout the microstructure with limited amount of planar slip and dissociated dislocations. The SEM-BSE images for

wrought 316, SR, SA and HIP heat-treated LPBF samples are shown in Fig. 2, where the typical microstructure of the wrought 316 can be seen in Fig. 2(a).

3.2.2. LPBF 316 powder characterisation

Representative SE/BSE images of the cross-section of the as-received 316 powder are shown in Fig. 3(a-c). Austenitic sub-grains with ~4 μm
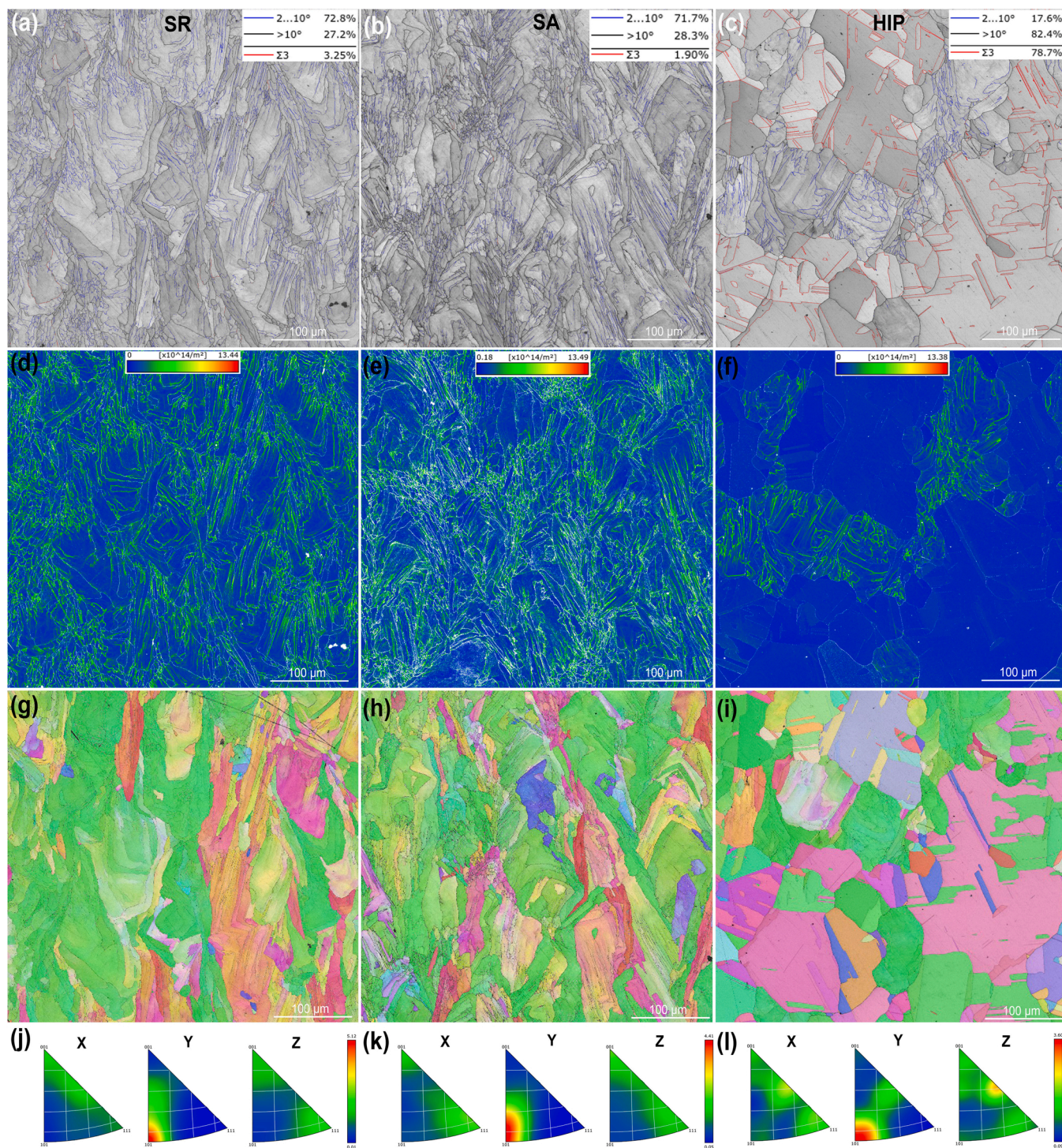
Fig. 4. (a-c) band contrast and grain boundaries overlaid maps, (d-f) GND distribution maps and (g-l) IPF maps for (a, d, g, j) SR, (b, e, h, k) SA and (c, f, i, l) HIP samples. The building direction is along the vertical direction of the images.

length and ~2.5 μm width were observed in Fig. 3(b-c). A large quantity of Cr-Mn oxides (verified by EDX) with average size of ~80 nm (both intra- and inter-granular) can be observed in Fig. 3(c). High-angle packet boundaries and low-angle sub-grain boundaries can also be distinguished (Fig. 3(d)). Around 1% of ferrite was present in the powder, mostly at the boundaries of the sub-grains (Fig. 3(c,e)). KAM is relatively low in the as-received 316 powder microstructure and the high local geometry necessary dislocation (GND) density seems to overlap with the sub-grain boundaries between 2 and 10°.

3.2.3. Microstructural characterisations of LPBF specimens

SEM-BSE images of the SR, SA and HIP treated samples are shown in Fig. 2(b-d), and the EBSD maps for the samples are shown in Fig. 4. BSE images show that the SR and SA samples have very similar fine-grained microstructure, and some grains were elongated in the direction with a small angle with the building direction (Fig. 2(b, c)). Duplexed grains were observed in the HIP sample, the size of the coarse grains is identical to that of the wrought material, and the coarse grains were surrounded by fine-grains (Fig. 2(d)). Fig. 4(a-f) show the band contrast and grain boundaries overlaid maps and GND density maps for different samples.

Columnar-shaped fine grains featuring orientation variation within them were observed in the SR sample. 72.8% of low-angle grain boundaries (LAGBs, 2–10°) and 27% of high-angle grain boundaries (HAGBs, >10°) were detected in this material with almost no twins (Fig. 4(a)). High GND density within the grains was revealed in this sample, as shown in Fig. 4(d). The average GND density of the sample was measured to be $1.95 \pm 1.05 \times 10^{14}/m^2$. In the SA sample, 71.7% LAGBs and 28.3% HAGBs were detected with nearly no twins. The GND density did not change significantly in comparison to that of SR sample ($1.76 \pm 1.07 \times 10^{14}/m^2$), which suggests that only recovery occurred during the annealing process (Fig. 4(b, e)). By analysing the pole figure, it is found that most of the grains were < 110 > oriented in the building direction for the SR and SA samples. It is worth mentioning that though the optical microscopy of etched specimens is not shown here for brevity, the melt pool boundaries in SR sample disappeared in the SA 316.

HIP induced significant change of the microstructure of the LPBF 316. Recrystallization occurred in most regions, leading to the formation of equiaxed grains and twins within them. The average recrystallized grain size was 80 μm. However, grains that did not experience recrystallization during the HIP process were also detected (Fig. 2(d) and Fig. 4(f)). EBSD analysis indicates that LAGBs and cellular structures with high GND density exist in these grains. The average GND density of this sample decreased to $0.65 \pm 0.57 \times 10^{14}/m^2$. In general, 17.6% LAGBs and 82.4% HAGBs were detected in the HIP sample. Of the HAGBs, 78.7% were confirmed to be twin boundaries. The HIP sample is more isotropic than the SR and SA samples because of the recrystallization process, and the grains are randomly oriented in all directions (Fig. 4(i)).

3.2.4. TEM analysis of LPBF specimens

TEM analyses of the AM specimens are shown in Fig. 5 and Fig. 6. Cellular structure with high-density dislocations tangled at the cell boundaries was observed within the grains of the SR sample, as shown in Fig. 5(a-c). The cell size in the sample is measured to be within ~400–600 nm. Based on the relationship between cell size and cooling rate of austenitic stainless steels, the cooling rate of the sample during printing was estimated to be in the range between $5 \times 10^6 - 5.7 \times 10^6$ °C/s [34]. Slight enrichment of Mo and Cr at the cellular walls was revealed *via* chemical analysis by STEM-EDX (Fig. 5(d-i)), and Fe is in
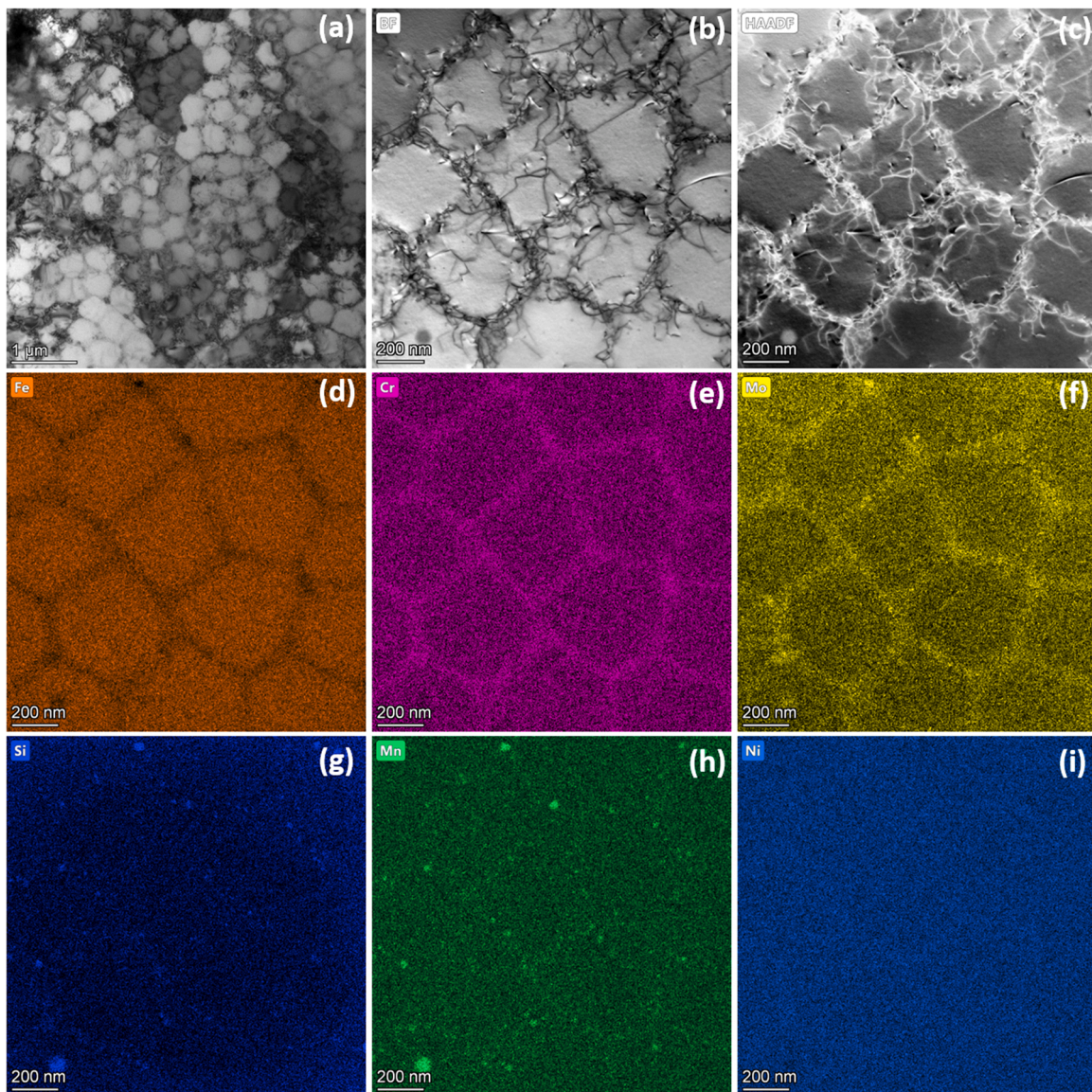

Fig. 5. (a) BF-TEM image of the cellular structure in SR sample; (b) B-STEM and (c) HAADF-STEM images of the cells, and (d-i) are the corresponding elemental distribution maps.
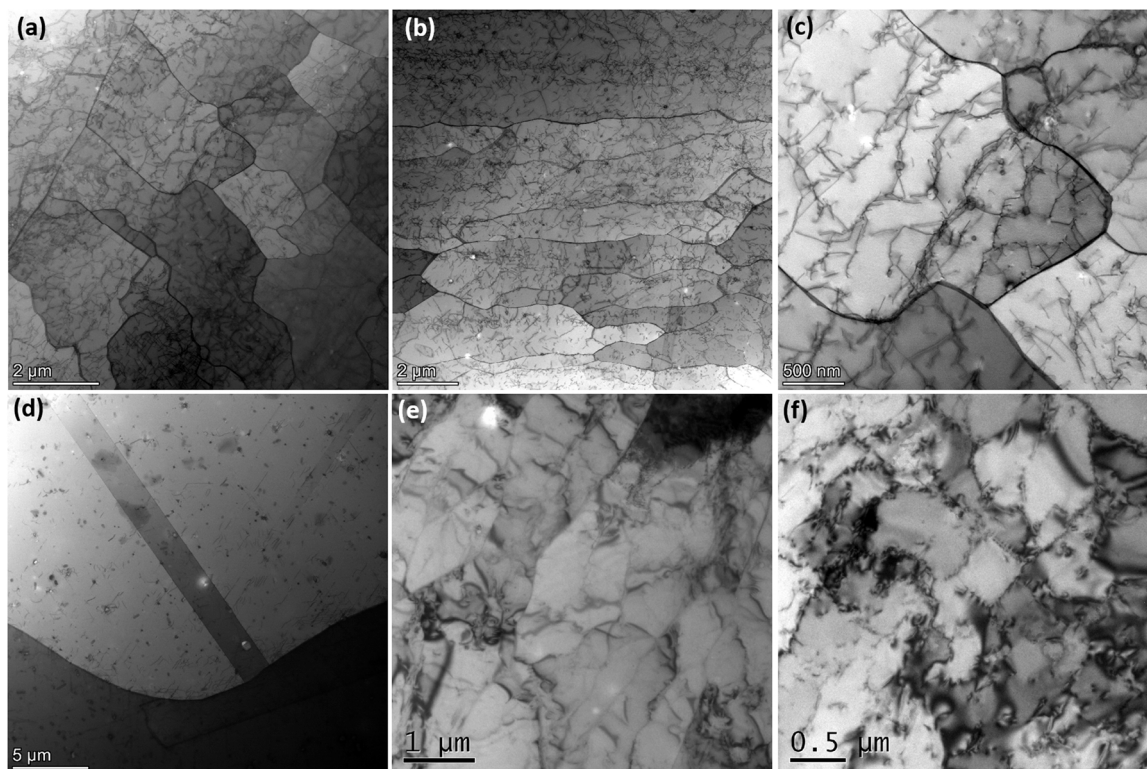
Fig. 6. (a-c) BF-STEM images of the SA sample; (d-f) BF-TEM images of the HIP sample. (d) was taken in a recrystallized grain and (e, f) were taken from a grain that did not experience fully recrystallization.

turn depleted at the cell walls. In addition, some Mn and Si-enriched oxides were also observed within the cell walls, as can be seen in Fig. 5(f-h). Ni is uniformly distributed in the material.

Cellular structure still existed in the LPBF stainless steel after the high-temperature SA treatment (Fig. 6(a-b)). However, the density of the dislocations at the cellular walls significantly decreased, leading to the disruption of the walls of some cells (Fig. 6(b-c)). HIP treatment led to partial recrystallization of the LPBF 316 (Fig. 4). Cellular structure disappeared in the recrystallized grains, as shown in Fig. 6(d). However, columnar grains and cellular structures still existed in some local partially recrystallized areas, where the dislocations at the cellular walls partially disappeared (Fig. 6(e-f)).

3.3. High-temperature electrochemical behaviour

3.3.1. EIS measurements

Typically, different processes in an electrochemical system have specific time constants to reach steady state when responding to sine-ewave voltage perturbation. The smaller the time constant, the higher the characteristic frequency of the process. Therefore, by measuring EIS in a broad range of frequencies (*e.g.* 10^5 to 10^{-4} Hz), an overview on the active processes in the system and their respective roles with regard to corrosion resistance is obtained. Moreover, corrosion resistance, associated with the polarization resistance of the system, is usually dominated by the processes occurring at the low-frequency end *i.e.* < 1 Hz.

As shown in Fig. 7 to Fig. 8, the high-frequency region (> 1 Hz) of electrochemical impedance (EI) spectra is broadly similar for all specimens. The EI spectra indicate that the wrought 316 specimen has a higher corrosion rate, which is evidenced by the lower impedance magnitude |Z| (*i.e.* lower polarisation resistance) than the LPBF specimens at the low-frequency end of the spectra. By careful deconvolution of the spectra, a total of four time constants are detected (marked by arrows in Fig. 7 to Fig. 8).

The highest frequency time constant is associated with the electronic

Fig. 7. EI spectra of the studied materials in (a) complex (parameter is frequency in Hz) and (b) Bode coordinates in the first EIS measurement. Points - experimental data, lines - best-fit calculation according to the MCM. Detected time constants were marked in the Bode phase angle plot with arrows.
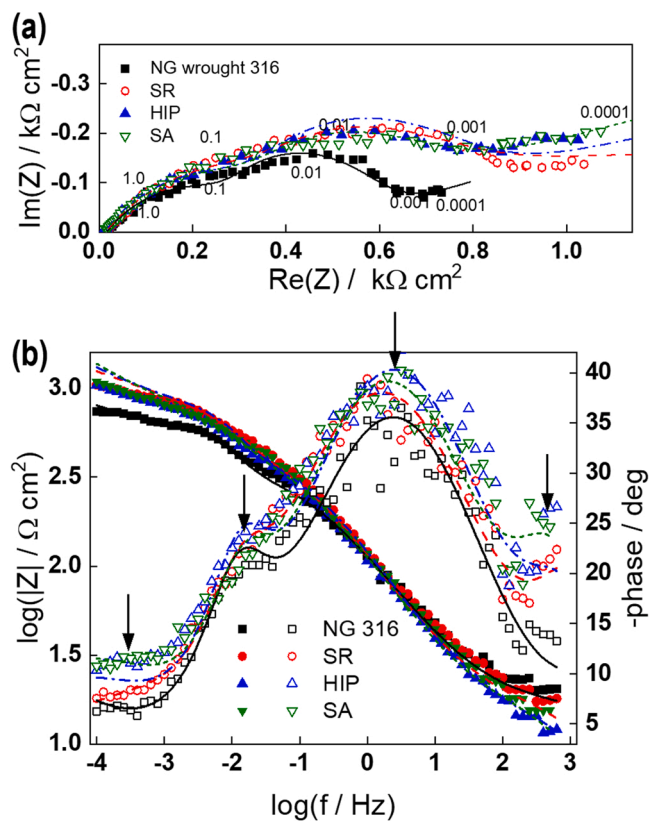
Fig. 8. EI spectra of the studied materials in (a) complex (parameter is frequency in Hz) and (b) Bode coordinates in the second EIS measurement. Points - experimental data, lines - best-fit calculation according to the MCM. Detected time constants were marked in the Bode phase angle plot with arrows.
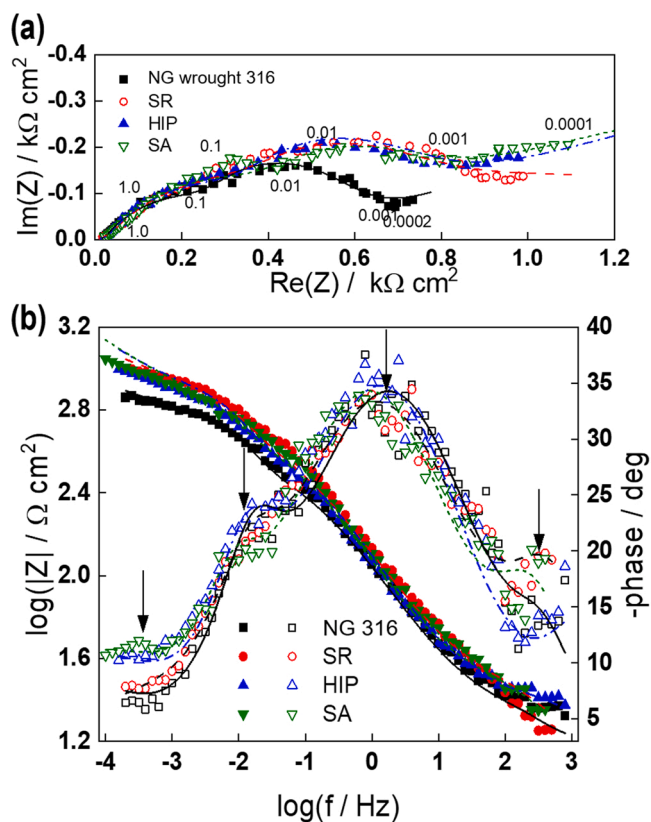
properties of the semiconducting oxide (barrier layer), the two intermediate time constants - with charge transfer and adsorption of intermediate products at the F/S interface, and at the low-frequency end, the data represent transport of ionic defects through the barrier part of the film.

3.3.2. Oxide film characterisation

SEM-SE images of the outer surfaces of LPBF and NG wrought 316 specimens after the exposure to high-temperature PWR environment are shown in Fig. 9. The outer surface oxide layers of the three heat-treated LPBF specimens reveal similar size of randomly distributed and disperse oxide particles. The highest surface coverage with an outer oxide layer was found in the NG wrought 316 specimen, indicating faster transport of ions through the inner oxide layer than in that of the heat-treated LPBF specimens.

The GDOES depth profiles of the LPBF 316 and NG wrought 316 specimens after exposure to high-temperature water are shown in Fig. 10. Typically, a contamination layer of ~50–60 nm containing relatively high amounts of adventitious carbon is observed on all specimens. An enrichment of Fe up to 57 at% at the depth of 100–150 nm was detected in the oxide on the NG wrought 316 specimen. At a distance of 500 nm from the surface, a peak for Cr concentration and a minimum of Fe content were observed. However, O concentration in oxide layers of the NG wrought 316 specimen is clearly higher than that in the oxides on heat-treated LPBF specimens. It was found that the O-profile can be described with two sigmoidal functions in the range 0.05–0.35 and 0.4–4 μm, which is indicative of a double-layer structure. The positions of the respective interfaces obtained by fitting is (1/2 height of O content) are indicated with vertical lines. In addition, Mn and Mo were found to be depleted in the oxide layer in comparison to their contents in the matrix, indicating preferential dissolution of those

elements. On the other hand, Si is slightly enriched in the oxide, indicating preferential oxidation. The profile of B shows a shallow maximum at the interface, thus it is slowly incorporated in the film during oxidation since it originates from the solution. The thicknesses of the barrier layer between the outer and inner oxide are ~100 nm for wrought 316 and ~50–60 nm for the LPBF specimens, whereas the thickness of the region between the inner oxide and the bulk alloy is ~200 nm. It is noteworthy that the Ni concentration at the F/S interface is clearly higher for the LPBF materials (around 10%) than in the wrought material (around 6.5%), which means there is less surface area for Fe to dissolve from the LPBF materials.

Cross-sectional SEM-BSE images of the outer and inner oxide layers of LPBF 316 and NG wrought 316 specimens after exposure to PWR environment are shown in Fig. 11. A continuous and dense inner oxide layer is present for the NG wrought 316 specimen. For the heat-treated LPBF specimens, disperse and non-uniform inner oxide layers were observed. At some locations, a very thin inner oxide layer of ~70 nm was present on the LPBF specimens, as shown in Fig. 11(f,i,l).

As revealed by the EDX mapping in Fig. 12, in both NG wrought 316 and HIP conditions, the inner oxide layers were depleted in Fe. The Cr content of inner oxide is higher than that both in the outer oxide layer and the bulk material. In contrast, Ni content in bulk material seems to be slightly higher than in the outer and inner oxide layers. Thus, a double-layer oxide structure composed of a Cr-enriched inner layer and a Fe-enriched outer layer is formed. Consistent results were revealed by the EDX line scan through the outer oxide, inner oxide and matrix of LPBF 316 and NG wrought 316 specimens in Fig. 13. The line scan results indicate that Cr concentration is marginally higher whereas Fe and Ni contents are slightly lower in inner oxide layer/crystals of LPBF materials when compared to the wrought 316 specimen.

3.3.3. EIS modelling

The EIS data was interpreted with the MCM to quantify the corrosion behaviour of investigated materials. The results from fitting of EI spectra to the transfer function (Eqs. (2)–(11)) are shown in Fig. 7 and Fig. 8 with solid lines and demonstrate the model capability to account for both the magnitude and frequency distribution of impedance with sufficient accuracy ($R^2 > 0.97$). Following the treatment in Refs. [31] an [32], the dielectric constant of the inner oxide, ε, and the part of the potential consumed at the F/S interface, α, were given values of 12 and 0.8, respectively. All the transfer coefficients of the individual steps of the hydrogen reaction, α_i, are assumed to be equal to 0.5 for simplicity. The values of all the parameters estimated from the fit and averaged between the first and second EIS measurement for each material together with the standard deviations are given in Table 4.

Several conclusions can be drawn from the values of kinetic parameters for the wrought material and the LPBF specimens. The parameters of alloy oxidation (k_O and k_M) at the inner interface are considerably lower for the LPBF specimens in comparison to the wrought 316 specimen, indicating a slower oxidation rate in comparison to the wrought material. Since under the assumption of a steady state, the rate of film formation is equal to that of oxide dissolution, it can be inferred that the oxide dissolution kinetics is significantly slower on the LPBF specimens. The rate constant of ejection of interstitial cations at the F/S interface is also considerably larger for wrought 316 with respect to the values for the LPBF materials, which points out to a higher corrosion release rate from the wrought material.

The parameters of the hydrogen evolution/oxidation reaction at the corrosion potential are practically independent on the type of material, indicating that electron conduction mechanism for all oxides is rather similar. This is in line with the similarity of the diffusion coefficient of electronic carriers for the oxides on all studied materials. Moreover, the field strength in the oxide and the diffusion coefficients of oxygen *via* vacancies and metal cations *via* interstitial positions in the spinel lattice are comparable for the four studied specimens, indicating that the ionic conduction mechanism in the oxide film is also rather similar.
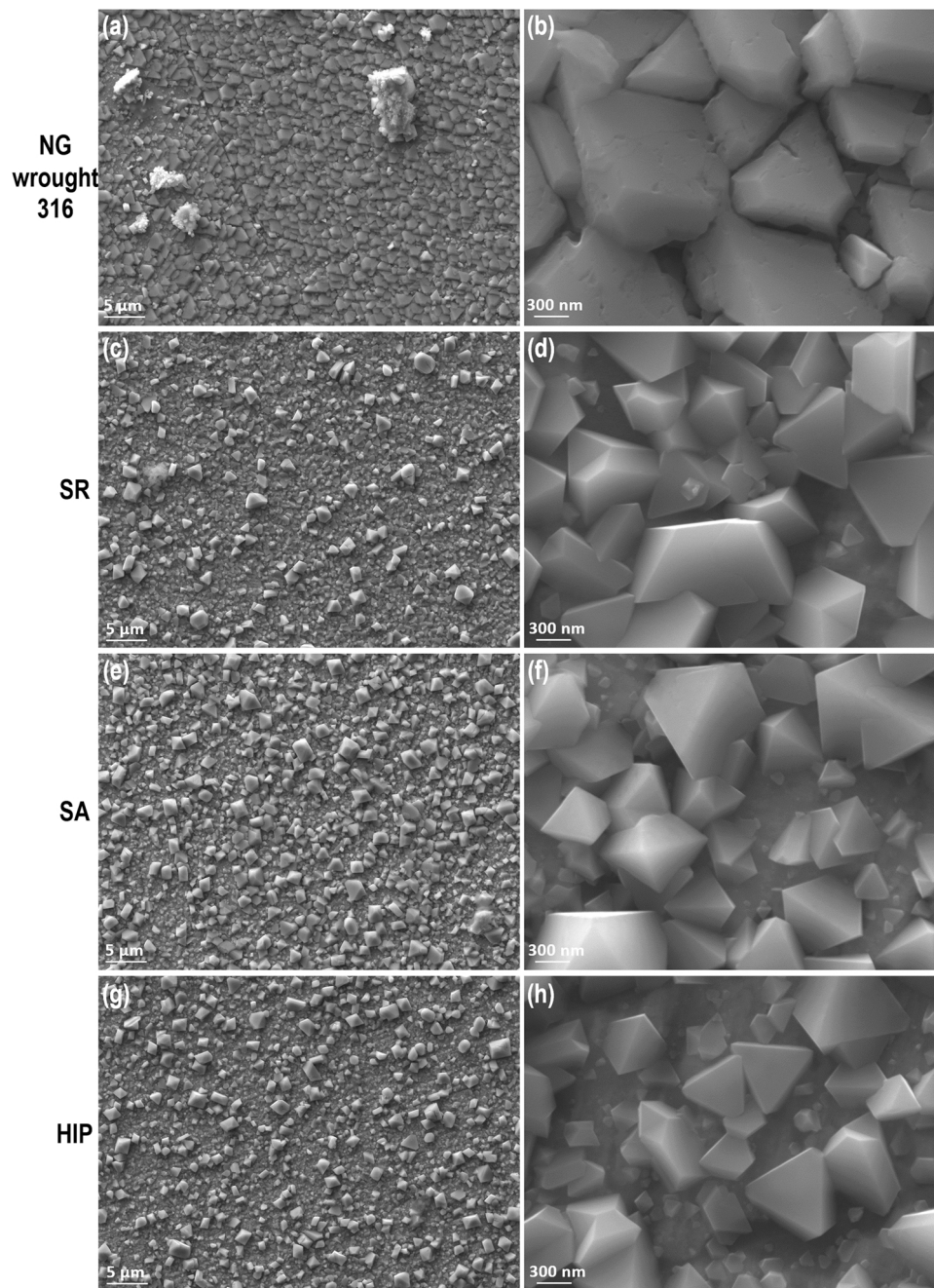
Fig. 9. SEM-SE images of the outer surfaces of LPBF 316 and NG wrought 316 specimens after the exposure to PWR environment. (a-b) Wrought 316; (c-d) SR; (e-f) SA; (g-h) HIP samples.

The thickness of the barrier part of the oxide (L) on the LPBF materials is considerably smaller to that on wrought 316 and comparable to that of the layer thickness estimated by GDOES on LPBF specimens (see Chapter 3.3.2). The capacitances of the space charge layer in the semiconducting phase of the oxide are smaller for the LPBF specimens than wrought 316. This may indicate a smaller number of ionic defects that are able to play the role of electron donors in the oxide when compared to wrought 316. The double layer capacitance $C_{F/S}$ does not depend on the type of material within the calculation error, whereas the values of the charge transfer resistance at the M/F interface R_t are rather small (indicating a fast process), calculated with a larger error and thus also indistinguishable between the different materials.

Summarizing, the post-LPBF heat-treated materials exhibit significantly different electrochemical behaviour than that of wrought 316.

Among the LPBF materials, SR sample shows only marginally lower corrosion and oxidation rates compared to those of SA and HIP samples.

4. Discussion

4.1. Evolution of microstructure and mechanical properties with heat treatments

Post-treatment is critical for AM materials/components to optimize their microstructure and mechanical properties. Microstructure of the LPBF 316 has changed after different heat treatments and these changes were correlated with the mechanical properties.

The SR treatment was conducted at relatively low temperature for a short period, therefore it was not able to significantly change the
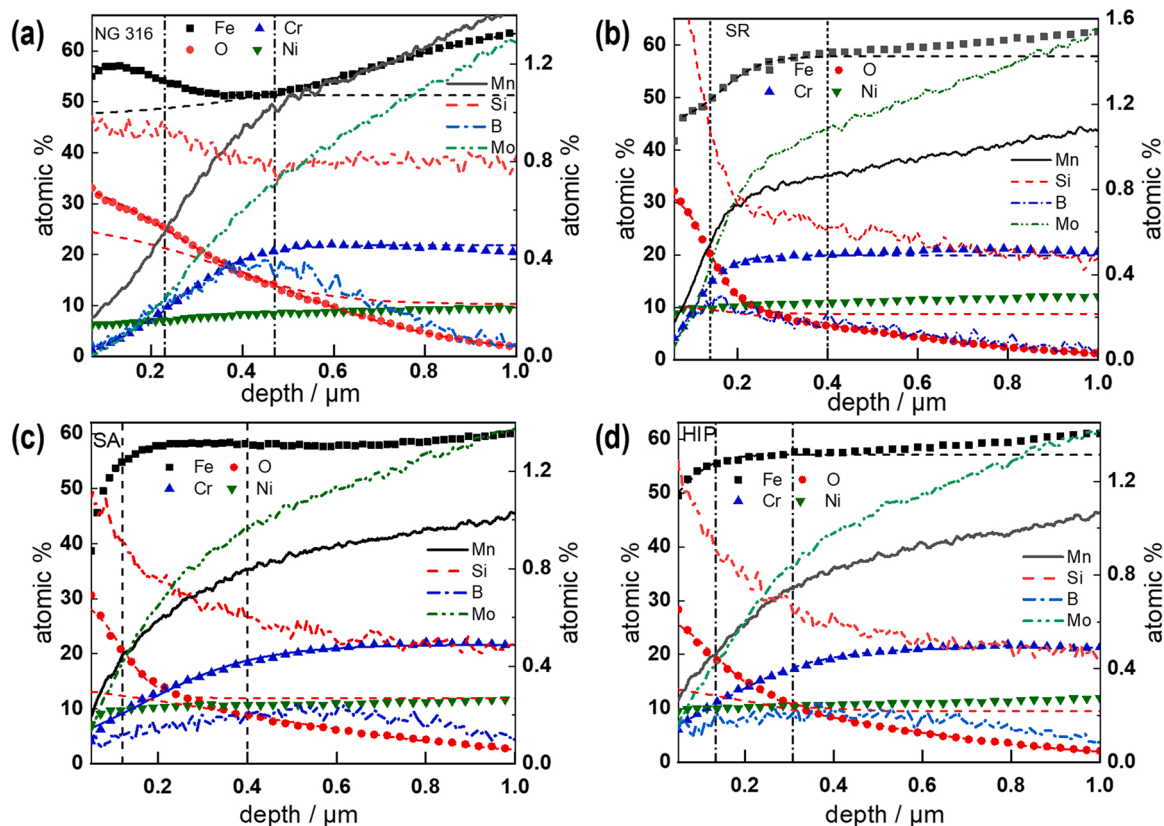
Fig. 10. GDOES depth profiles with atomic concentrations of constituent elements of LPBF 316 and NG wrought 316 specimens after exposure to PWR environment. (a) Wrought 316; (b) SR; (c) SA and (d) HIP samples.

microstructure of the LPBF 316. As revealed by EBSD and TEM (Fig. 4 to Fig. 6), SR sample has highly-textured grains in the building direction and ~70% of the grain boundaries were determined to be LAGBs (2–10°). The grains which were [011]-orientated in the building direction were formed as a result of the specific thermal dissipation of the melting pool induced by the laser. The preferential growth direction for face-centered cubic structured materials is [001] direction, which is usually in the opposite direction of the heat dissipation of the melt. In addition, the heat dissipation direction for the melt is always perpendicular to the building direction. As the melting pool induced by laser has hemisphere/ hemi-ellipse morphology, the pool boundary always has an angle with the building direction. The angle between [011] and [001] directions is 45°, and therefore most of the grains in the SR LPBF 316 are preferentially oriented along [011] direction or close to [011] direction. In addition, cellular structures with high-density dislocations and slightly element segregation were observed within the grains in the SR LPBF 316 [11]. The cellular structures were formed due to the cellular solidification of the melt induced by the high cooling rate during the rapid scanning process [34,35].

Room temperature yield strength for wrought and annealed NG 316 is usually 200–300 MPa. However, the strength for the SR 316 sample is much higher than that of the wrought material (Table 1). Finer grain size is one of the main reasons. The grain size for wrought and annealed 316 is usually dozens to hundred microns, whilst the grain size of LPBF 316 is several microns (with the contribution of the LAGBs, Fig. 4 and Fig. 5). In addition to the contribution of the grain boundaries, the cell walls which are tangled with dislocations and enriched with Mo and some Cr can also hinder the movement of dislocations, promote twining deformation, and then increase the yield strength, which have been observed by Wang et al. [36]. However, the contribution of the cell walls should be less than that of the LAGBs because the cell walls do not induce change in orientation, and planar slip and twining can still go across

them [36]. Furthermore, the nano-sized oxides can also provide dispersion strengthening effect to LPBF material. The nano-sized oxides are unique in the LPBF 316 in comparison with their wrought counterpart, which origin from the oxygen absorbed at the powder surface and the oxygen in the argon gas used to protect the melting pool during printing process [1].

High-temperature annealing at ~1050 °C is usually used to induce complete recrystallization of forged or rolled 316. However, it is found that this annealing process only led to the recovery of the LPBF 316. The grain structure for the SA sample is similar to that of the SR sample, with ~70% of the grain boundaries are LAGBs and most of the grains were < 110 > orientated in the building direction. The only difference is that the density of the dislocations at the cell walls was reduced in SA sample than in the SR sample and some cell boundaries disappeared/got interrupted due to dislocation movement driven by temperature, as revealed by TEM analysis (Fig. 6(a-c)). In fact, the main driving force for recrystallization in conventionally forged materials is the static stored energy in the form of high-density dislocation, which leads to significant misorientation within the deformed grains. Lots of dislocations were also observed in the LPBF 316, but they were formed as a result of solidification and do not lead to misorientation within the grains, therefore cannot provide enough driving force for recrystallization. These results further confirm the observations of the high stability of the cell structure in AM 316 at high temperature by other researchers, such as Salman et al. [21] and Chen et al. [37]. The slightly decrease in yield strength and toughness of the SA sample is due to the movement of the dislocations at the cell walls which leads to the disruption.

The isostatic high pressure which is applied to the material *via* argon gas during HIP is able to induce plastic deformation and promote diffusion creep of the material when there are closed internal pores in the material [38]. For LPBF 316 in this study, the 0.3% pores were closed with HIP, which is expected to increase the SCC or corrosion fatigue
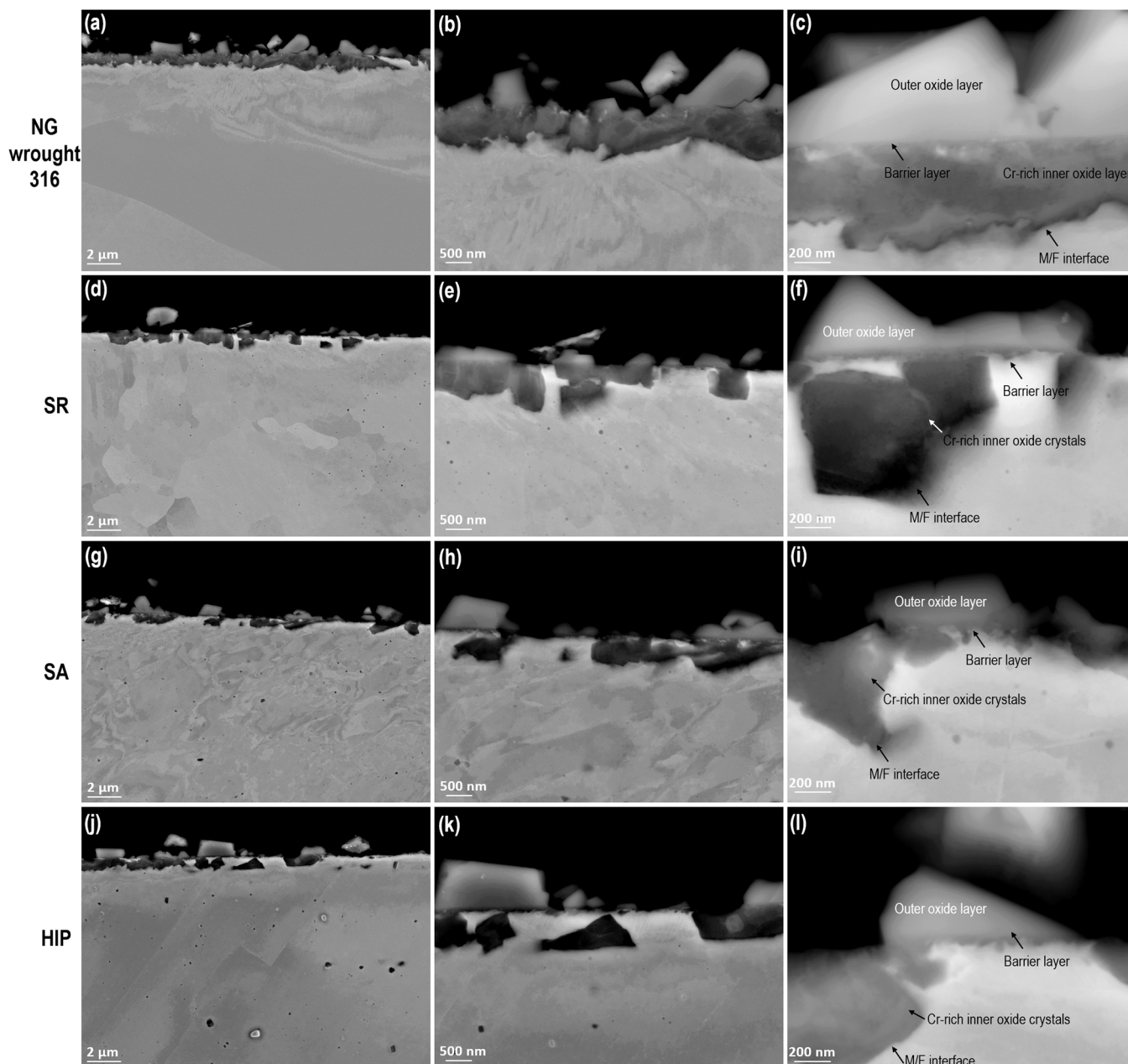
Fig. 11. Cross-sectional SEM-BSE images of the outer and inner oxide layers of LPBF 316 and NG wrought 316 specimens after the exposure to PWR environment. (a-c) Wrought 316; (d-f) SR; (g-i) SA; (j-l) HIP samples.

properties of the material in high-temperature water environment. The higher temperature and longer duration during HIP induce dramatic changes in microstructure of the material. Recrystallization happened during HIP, which lead to elimination of most of the LAGBs, cell structures, and coarsening of the grain size. These microstructure changes leads to a sharp decrease of both the yield strength and toughness of the material. In addition, another reason for the reduction in impact energy is the coarsening of oxides due to heat treatments since the oxides act as microvoid initiation sites. LAGBs and dislocations still exist in some grains even after HIPing at 1150 °C/4 h, which further indicates that the cell structures are very stable. In fact, it has been reported that the cells in AM 316 can only be eliminated when the heat treatment/HIPing temperature is higher than 1200 °C [33].

4.2. Correlation of LPBF microstructure with electrochemical behaviour

The EIS measurements in 288 °C high-temperature PWR water and the associated modelling revealed a different electrochemical response of the four investigated materials, particularly during comparison of wrought and LPBF samples. In the following, a correlation between high-temperature electrochemical behaviour and microstructure is sought for.

4.2.1. Microstructural factors

Microstructural factors (like boundaries, cell structures, precipitates and dislocations) that might contribute to the variation in electrochemical behaviour are discussed in the following paragraphs.

Melt pool boundaries of the LPBF 316 disappeared after the SA or HIP treatments. Inhomogeneous high-energy microstructural defects, pores, residual stress, local heat-affected zone and unstable non-metallic
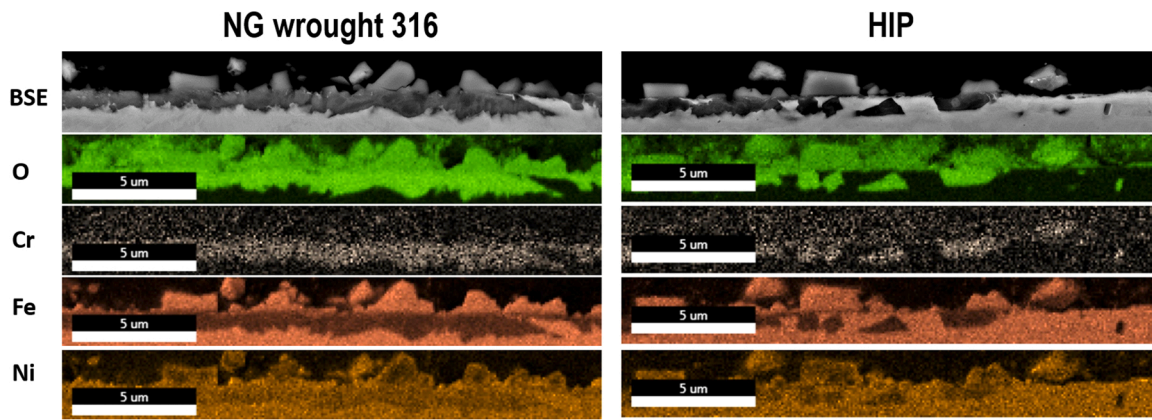
NG wrought 316

HIP

Fig. 12. SEM-BSE images and EDX of the outer and inner oxide layers of NG wrought 316 and HIP treated LPBF 316 specimens after the exposure to PWR environment.
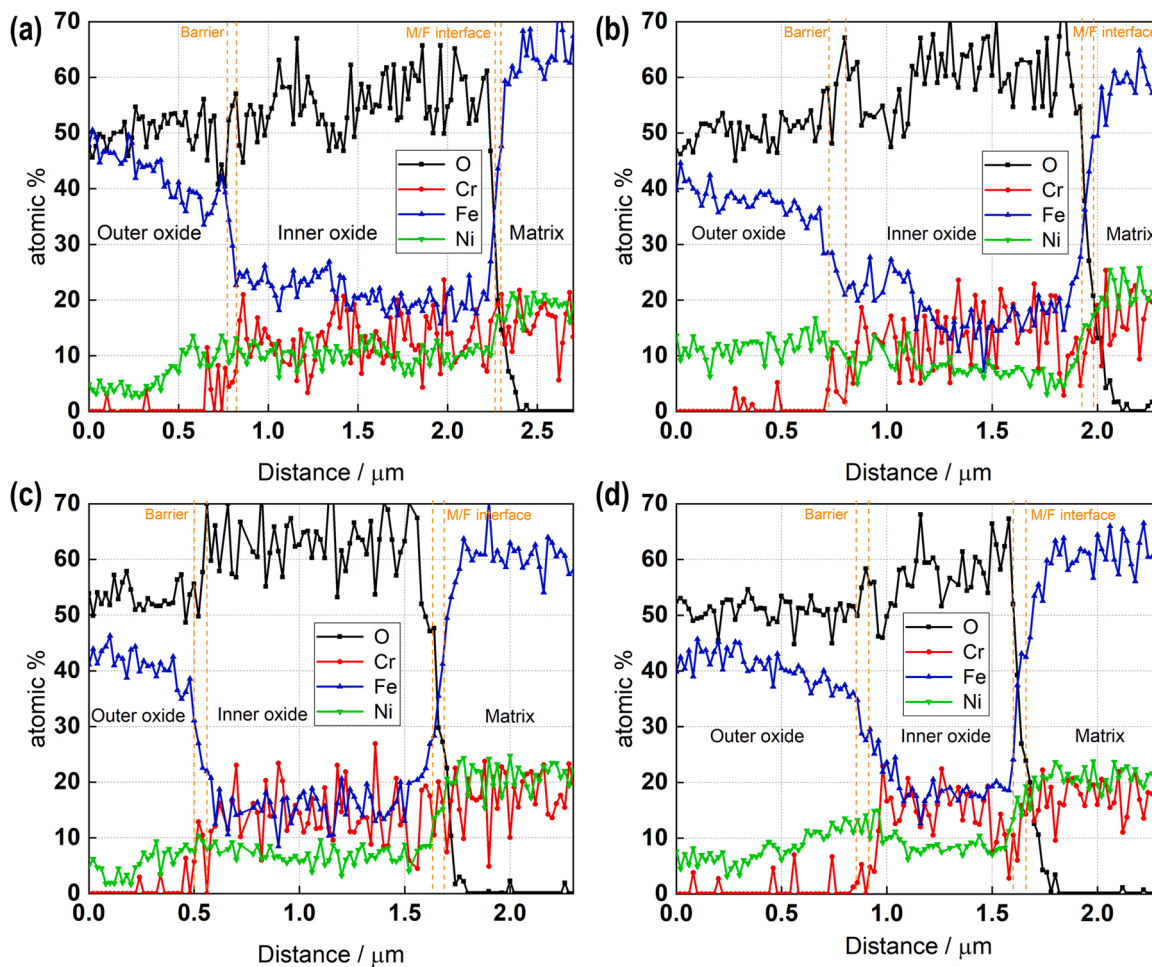

Fig. 13. Line EDX through the outer oxide, inner oxide and matrix of LPBF 316 and reference NG wrought 316 specimens after the exposure to PWR environment. (a) Wrought 316; (b) SR; (c) SA; (d) HIP samples. Note the line EDX in (b-d) of LPBF materials was chosen to scan through locations with inner oxide crystals.

elements normally concentrate in the melt pool boundaries, which make them candidate weak regions in LPBF 316 samples. The pitting potential of samples after heat treatment at 950–1100 °C were reported to be higher than that of the as-printed specimens due to the dissolution of the melt pool boundaries [39]. However, as shown by the EI spectra, the SA and HIP heat-treated samples exhibited slightly higher corrosion rates in high-temperature water than the SR sample. This implies that the disappearance of melt pool boundaries might not be the major

influencing factor on high-temperature electrochemical behaviour.

Grain boundaries promote diffusion, inward oxidation and formation of crystals in the inner oxide layer for both LPBF and wrought 316. Compared with the coarse recrystallized grains of ~80 μm in HIP 316, the grains in the SR sample are one order of magnitude smaller. Thus, the grain boundary density in studied materials ranks as SR > SA > HIP ≥ wrought 316. However, the number of distributed inner oxide Cr-rich crystals in HIP sample is not significantly lower than in SR or SA

Table 4

Kinetic parameters estimated from the fitting of the EIS data to the equations of the MCM.

Parameters	Wrought 316	SR	SA	HIP
$10^{11} k_M$ / mol cm^{-2} s^{-1}	15 ± 1.2	6.1 ± 0.6	8.0 ± 0.6	7.1 ± 0.7
$10^{11} k_O$ / mol cm^{-2} s^{-1}	10 ± 0.8	4.2 ± 0.5	5.0 ± 0.5	5.0 ± 0.5
C_{sc} / μF cm^{-2}	22 ± 1.0	11 ± 1.0	20 ± 1.0	16 ± 1.0
L / nm	78 ± 5.0	47 ± 2.0	52 ± 2.0	51 ± 2.0
$10^8 D_e$ / cm^2 s^{-1}	5.0 ± 0.5	5.3 ± 0.5	5.6 ± 0.6	5.4 ± 0.6
R_t / Ω cm^2	2.8 ± 1.0	5.6 ± 1.5	5.1 ± 1.5	5.3 ± 1.5
$C_{F/S}$ / mF cm^{-2}	2.8 ± 0.006	3.1 ± 0.006	3.6 ± 0.007	2.6 ± 0.007
$10^9 k_{2M}$ / cm s^{-1}	4.5 ± 0.2	2.2 ± 0.1	3.0 ± 0.1	3.5 ± 0.1
$10^9 k_{2O}$ / cm s^{-1}	2.0 ± 0.1	2.0 ± 0.1	2.0 ± 0.1	2.2 ± 0.1
$10^{10} k_{1H}$ / mol cm^{-2} s^{-1}	1.1 ± 0.1	1.10 ± 0.1	1.0 ± 0.1	1.1 ± 0.1
$10^{10} k_{2H}$ / mol cm^{-2} s^{-1}	1.2 ± 0.1	1.2 ± 0.1	1.2 ± 0.1	1.2 ± 0.1
$10^{10} k_{-1H}$ / mol cm^{-2} s^{-1}	1.3 ± 0.1	1.3 ± 0.1	1.3 ± 0.1	1.3 ± 0.1
$10^4 k_{-2H}$ / cm s^{-1}	1.4 ± 0.1	1.4 ± 0.1	1.4 ± 0.1	1.4 ± 0.1
$β$ / nmol cm^{-2}	4.9 ± 0.4	4.7 ± 0.4	4.6 ± 0.4	3.9 ± 0.4
$10^{17} D_M$ / cm^2 s^{-1}	5.0 ± 1.0	4.5 ± 1.0	5.0 ± 1.0	4.5 ± 1.0
$10^{17} D_O$ / cm^2 s^{-1}	4.0 ± 1.0	4.0 ± 1.0	4.5 ± 1.0	4.0 ± 1.0
$\vec{E}$ / kV cm^{-1}	109 ± 5.0	106 ± 5.0	106 ± 5.0	104 ± 5.0

materials (as revealed by Fig. 11), and there is a huge difference in the inner oxide structure between the HIP and wrought 316, which indicates a minor direct role of grain boundaries on electrochemical behaviour.

The cellular sub-grain structure of ~400–600 nm in SR sample has a high dislocation density. As revealed by the TEM studies, the cellular boundaries are partly dissolved in the SA sample with dislocations movement/annihilation and mostly eliminated in the HIP sample. In this work, the SR sample exhibited marginally lower corrosion rates in high-temperature water than the other post-LPBF heat-treated materials. This is in agreement with the finding of Zhou et al. [39] that after recrystallization at 1100 °C, corrosion resistance was weakened with the reduced LAGB and cell boundary density, re-precipitation and increased segregation. The cellular structure with high dislocation density in SR sample could form an interconnected 3D network, contribute to the passivity and enhance the growth of a passive oxide film, which inhibits corrosion into the matrix. With the partial disappearance of cellular structure and decrease in dislocation density in SA and HIP conditions, the corrosion rate slightly increases compared to SR sample.

The main microstructural factor resulting in the different electrochemical response between the LPBF materials and the wrought 316 is possibly the nano-precipitate. The chemical compositions of the impact toughness specimens were measured by OES and the O content is around 250 wppm for all three post-LPBF heat-treated specimens. Even if the size of precipitates increased after the SA and HIP heat treatments, as revealed by the cross-sectional SEM images of post-exposure samples (Fig. 11), a considerable amount of circular nano-precipitates smaller than ~200–500 nm still exist in the grains after HIP. In that respect, the work by Sander [40] and Chao [41] demonstrated the less detrimental effect of nanoscale oxide inclusions formed during LPBF on pitting corrosion of LPBF 316 when compared to that of a wrought 316.

4.2.2. Electrochemical behaviour in PWR water

LPBF 316 specimens were reported to show a wider passive range than the wrought material, which is attributed to a finer microstructure and a native oxide with higher stability [42]. The passive film on LPBF 316 specimens has shown better barrier properties and increased pitting resistance than that on wrought specimens [43,44]. Man et al. [45] reported that the cell boundaries result in a more stable and continuous passive film by increasing the number of nucleation sites. Though these studies on corrosion behaviour were not conducted in high-temperature water, they are in line with this work in that the LPBF 316 seems to

possess a better corrosion resistance than wrought 316. However, different roles of the post-LPBF heat treatments on electrochemical behaviour have been described in the literature. Ettefagh et al. [46] reported that LPBF samples have an improved corrosion behaviour over the traditional counterparts and the heat treatment processes reduce the corrosion rate of the LPBF samples. Kong et al. [47] reported that the passive film thickness and corrosion potential of the LPBF 316 stainless steel decreased after recrystallization heat treatments at 1050 °C and at 1200 °C. In this work, the differences between the post-LPBF heat-treated 316 materials are only marginal.

The formation of a passive layer on austenitic stainless steels in PWR environment is a key phenomenon in explaining their SCC susceptibility [48]. As revealed by the EIS modelling, the parameters of the hydrogen evolution/oxidation reaction, the field strength in the oxide film and the diffusion coefficient of electronic carriers for the oxides are comparable for the four materials studied. This indicates that the electron and ion conduction mechanisms in the oxide film on all studied materials are rather similar. However, the parameters of alloy oxidation at the M/F interface and the rate constant of ejection of interstitial cations at the F/S interface are considerably lower for the LPBF specimens in comparison to the wrought 316 material. This points to a significantly slower oxide dissolution kinetics resulting in lower oxidation and corrosion release rates from the LPBF specimens in comparison to the wrought material. Furthermore, the smaller capacitances of the space charge layer in the semiconducting phase of the oxide of the LPBF specimens infer a smaller number of ionic defects and electron donors in the oxide compared to wrought 316. The thickness of the barrier part of the inner oxide layer on the LPBF materials (as estimated based on the EIS results) is estimated to be considerably lower than that on wrought 316, about 50 nm and 80 nm, respectively. The cationic composition of the inner layer as a spinel oxide of the type $(Ni_xFe_{1-x})(Cr_yFe_{1-y})_2O_4$ is available from GDOES, and using the normalized metal fractions, the following stoichiometries can be inferred: for the reference material, $(Ni_{0.31}Fe_{0.69})(Cr_{0.18}Fe_{0.82})_2O_4$, and for the SA, SR, and HIP alloys - $(Ni_{0.37}Fe_{0.63})(Cr_{0.32}Fe_{0.68})_2O_4$. Thus the spinel oxide formed on the AM alloys contains more Cr in octahedral and Ni in tetrahedral positions when compared to reference material.

Obviously GDOES, averaging laterally over an area with a diameter of 2.5 mm and significantly influenced by surface flatness, would not be sensitive to local sub-micrometre scale details. EIS, on the other hand, although also an averaging technique, would be expected to reveal the influence of such details, provided that the electrochemical processes are heavily concentrated locally. This is confirmed by post-exposure cross-sectional microscopy that points to an inhomogeneous inner oxide layer on the three heat-treated LPBF materials, which is different from the uniform inner oxide layer on the wrought 316. In the post-LPBF heat-treated materials, the inner oxide crystals rich in Cr have apparently grown only locally, suggesting local electrochemical reactions and high local rates of cation transfer. Nano-precipitates enriched in Mo, Cr, Si and O found in the original microstructure of LPBF materials are likely to be responsible for the highly localized growth of the Cr-rich oxide crystals. The preferential nucleation of Cr-rich oxides at the nano-precipitates was reported by Bertali et al. [49] based on the observation of discrete nano-scale oxide 'core' within the Cr_2O_3 in PWR water. The Mo-rich nano-precipitates will become the anodic site due to a higher electrochemical activity. Similarly, the Cr-depleted immediate surrounding areas of Cr-rich nano-precipitates will become anodic sites in high-temperature water. Zhou et al. [39], Shimada et al. [50] and Laleh et al. [27] also reported that re-precipitation or coarsening of the precipitates can offset some of the corrosion resistance by local elemental depletion from the neighbouring areas.

The electrochemical processes and the formation of outer and inner oxide layers of wrought 316 and LPBF 316 in PWR environment are depicted in Fig. 14. In PWR primary water environment with sufficient amount of dissolved hydrogen, Ni will stay in metallic form, and thus the higher Ni content at the F/S interface in LPBF 316 (Fig. 10) limits the
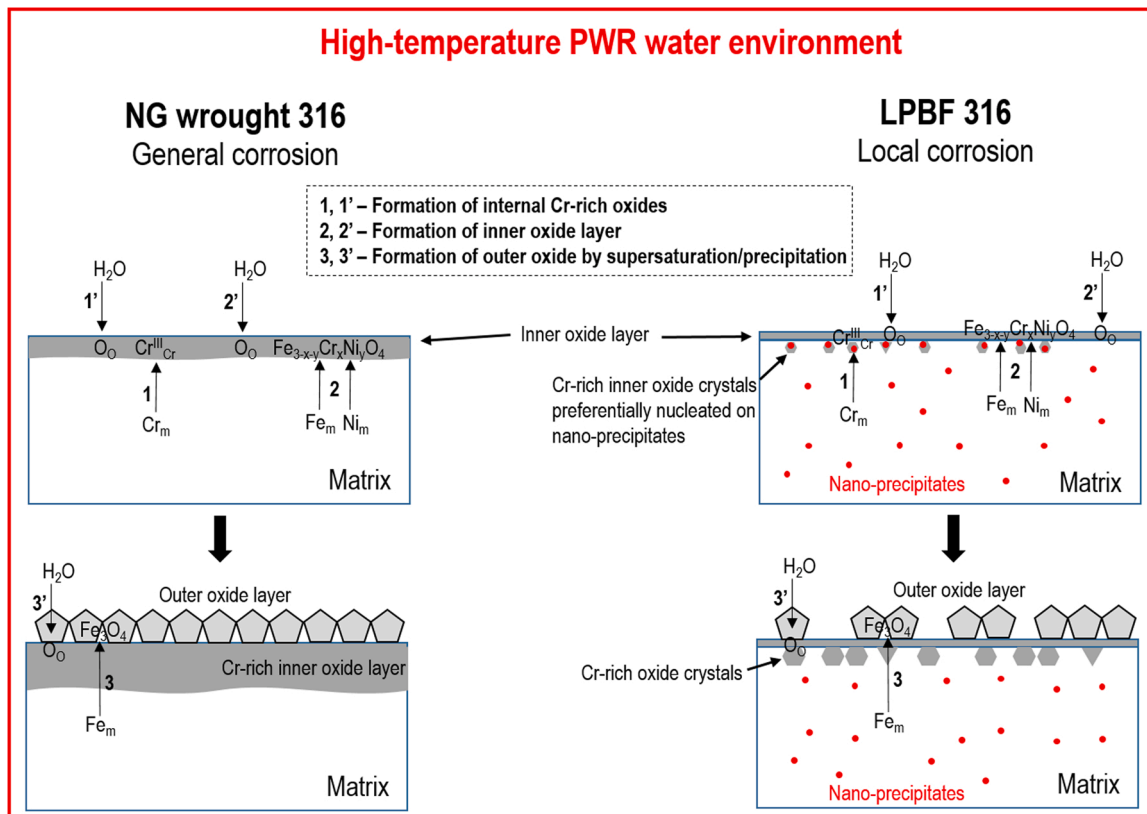
Fig. 14. The electrochemical processes and the formation of structure of outer and inner oxide layers of NG wrought 316 and LPBF 316 specimens in PWR environment.

possibility of Fe dissolution. Since Ni catalyses hydrogen oxidation [51, 52], the higher Ni concentration of LPBF materials (Table 1) could result in a locally higher hydrogen oxidation rate (*i.e.* anodic reaction rate) near the locations of the nano-precipitates, thus further slowing down the other anodic reactions in these areas. This is due to the fact that in an open circuit, the sum of all anodic currents (hydrogen oxidation and Fe dissolution) should be equal to the sum of cathodic currents (reduction of water being the only cathodic reaction). This redistribution of reaction rates could keep the anodic activity of the LPBF materials localized at the nano-precipitate sites and contribute to the formation of the sparsely distributed inner Cr-rich oxide crystals instead of a more uniform inner oxide layer.

On the wrought 316 material, the processes are more like in the form of general corrosion. At the early stage of exposure, tiny Cr-rich oxide nuclei are formed (process 1 and 1′), followed by the formation of uniform inner oxide layer (process 2 and 2′). Subsequently, outer oxide layer is formed at the F/S interface by supersaturation/precipitation (process 3). For LPBF materials, the electrochemical processes 1 and 1′ are of more localised nature than on wrought 316. The Cr-rich oxides nucleate preferentially at the nano-precipitates and their immediate surroundings close to the M/F interface. The growth of Cr-rich oxide crystals encloses the nano-precipitates, keeping the initiation site anodically active until the inner oxide diameter locally reaches its steady-state limit. Simultaneously with reactions 1 and 1′, reactions 2 and 2′ take place at a smaller fraction at the M/F interface, resulting in a thin inner oxide layer with a decreased kinetics of passive film growth in high-temperature water. Consequently, process 3 takes place at a smaller fraction of the surface, leading to less outer layer oxide crystals than on the wrought 316 material (with lower rates of dissolution, saturation and oxide precipitation).

5. Conclusions

The effect of post heat treatments on the high-temperature electrochemical behaviour, microstructure and mechanical properties of LPBF 316 was investigated using NG wrought 316 as reference. The following conclusions can be drawn from the obtained results:

- The yield strength and impact toughness are ranked as SR > SA > HIP > wrought 316. The superior mechanical properties of the LPBF specimens are mainly attributed to the cellular structures with large amounts of dislocations and LAGBs formed during sample building. The disappearance of the cellular structures, decrease in dislocation density and occurrence of recrystallization explains the lower flow stress and impact energy but higher fracture elongation of the SA and HIP samples compared to the SR sample. The tensile and impact properties of LPBF 316 meet the requirements for nuclear components.
- The high-temperature EIS results at 288 °C and their modelling indicate a considerably faster oxide dissolution kinetics and corrosion rate of wrought 316 when compared to LPBF 316. Barrier layers on LPBF specimens contain a smaller number of ionic defects acting as electron donors and exhibit lower oxide formation and corrosion release rates than on wrought 316.
- An inhomogeneous inner oxide layer is formed on post LPBF treated 316, in contrast to the uniform inner oxide layer on wrought 316. The thickness of the barrier part of the oxide on LPBF 316 is considerably smaller to that on the wrought 316. The localised nature of the electrochemical processes is suggested to be induced by the local anodic activity caused by the nano-precipitates in the LPBF 316.

- Despite a significant difference in microstructure, SR treated LPBF 316 shows only marginally lower corrosion rate compared to SA and HIP treated LPBF 316.

CRediT authorship contribution statement

Litao Chang: Writing – review & editing, Writing – original draft, Methodology, Investigation, Formal analysis, Data curation. **Timo Saario:** Writing – review & editing, Methodology, Investigation, Formal analysis, Data curation. **Zaiqing Que:** Writing – review & editing, Writing – original draft, Resources, Project administration, Methodology, Investigation, Formal analysis, Data curation, Conceptualization. **Martin Bojinov:** Writing – review & editing, Methodology, Investigation, Formal analysis, Data curation, Conceptualization.

Declaration of Competing Interest

The authors declare that they have no known competing financial interests or personal relationships that could have appeared to influence the work reported in this paper.

Data Availability

The data that support the findings of this study are available from the corresponding author upon reasonable request.

Acknowledgements

References

[1] H. Springer, C. Baron, A. Szczepaniak, E. Jägle, M. Wilms, A. Weisheit, D. Raabe, Efficient additive manufacturing production of oxide- and nitride-dispersion-strengthened materials through atmospheric reactions in liquid metal deposition, Mater. Des. vol. 111 (2016) 60–69.

[2] G. Wang, H. Ouyang, C. Fan, Q. Guo, Z. Li, W. Yan, Z. Li, The origin of high-density dislocations in additively manufactured metals, Mater. Res. Lett. vol. 8 (8) (2020) 283–290.

[3] "Roadmap for Regulatory Acceptance of Advanced Manufacturing Methods in the Nuclear Energy Industry," Nuclear Energy Institute, 2019.

[4] M. Hiser, A. Schneider, M. Audrain, A. Hull, Regulatory research perspective on additive manufacturing for nuclear component applications, J. Nucl. Mater. vol. 546 (152726) (2021), 152726.

[5] US Department of Energy, 2022. [Online]. Available: ⟨https://www.energy.gov/ne/articles/tva-installs-3d-printed-fuel-assembly-brackets-commercial-reactor⟩.

[6] D. Kong, C. Dong, S. Wei, X. Ni, L. Zhang, R. Li, L. Wang, C. Man, X. Li, About metastable cellular structure in additively manufactured austenitic stainless steels, Addit. Manuf. vol. 38 (101804) (2021), 101804.

[7] T. Ngo, A. Kashani, G. Imbalzano, K. Nguyen, D. Hui, Additive manufacturing (3D printing): a review of materials, methods, applications and challenges, Compos. Part B vol. 143 (2018) 172–196.

[8] Y. Sun, A. Moroz, K. Alrbaey, Sliding wear characteristics and corrosion behaviour of selective laser melted 316L stainless steel, J. Mater. Eng. Perform. vol. 23 (2014) 518–526.

[9] Z. Sun, X. Tan, S. Tor, Selective laser melting of stainless steel 316L with low porosity and high build rates, Mater. Des. vol. 104 (2016) 197–204.

[10] W. Tucho, V. Lysne, H. Austbø, A. Sjolyst-Kverneland, V. Hansen, Investigation of effects of process parameters on microstructure and hardness of SLM manufactured SS316L, J. Alloy. Compd. vol. 740 (2018) 910–925.

[11] T. Kurzynowski, K. Gruber, W. Stopyra, B. Kuźnicka, E. Chlebus, Correlation between process parameters, microstructure and properties of 316 L stainless steel processed by selective laser melting, Mater. Sci. Eng. A vol. 718 (2018) 64–73.

[12] R. Belles, W. Poore, T. Harrison, M. Muhlheim, T. Muth, A Survey of Additive Manufacturing Capabilities, ORNL/TM- 2018/1013 (2018).

[13] J. Reijonen, R. Björkstrand, T. Riipinen, Z. Que, S. Metsä-Kortelainen, M. Salmi, Cross-testing laser powder bed fusion production machines and powders: variability in mechanical properties of heat-treated 316L stainless steel, Mater. Des. vol. 204 (109684) (2021).

[14] M. Godec, S. Zaefferer, B. Podgornik, M. Šinko, E. Tchernychova, Quantitative multiscale correlative microstructure analysis of additive manufacturing of stainless steel 316L processed by selective laser melting, Mater. Charact. vol. 160 (110074) (2020), 110074.

[15] P. Tang, H. Xie, S. Wang, X. Ding, Q. Zhang, H. Ma, J. Yang, S. Fan, M. Long, D. Chen, X. Duan, Numerical analysis of molten pool behavior and spatter formation with evaporation during selective laser melting of 316L stainless steel, Metall. Mater. Trans. B vol. 50B (2019) 2273–2283.

[16] Z. Li, T. Voisin, J. Mckeown, J. Ye, T. Braun, C. Kamath, W. King, Y. Wang, Tensile properties, strain rate sensitivity, and activation volume of additively manufactured 316L stainless steels, Int. J. Plast. vol. 120 (2019) 395–410.

[17] Y. Kok, X. Tan, P. Wang, M. Nai, N. Loh, E. Liu, S. Tor, Anisotropy and heterogeneity of microstructure and mechanical properties in metal additive manufacturing: a critical review, Mater. Des. vol. 139 (2018) 565–586.

[18] X. Lou, M. Othon, R. Rebak, Corrosion fatigue crack growth of laser additively-manufactured 316L stainless steel in high temperature water, Corros. Sci. vol. 127 (2017) 120–130.

[19] X. Lou, M. Song, P. Emigh, M. Othon, P. Andresen, On the stress corrosion crack growth behaviour in high temperature water of 316L stainless steel made by laser powder bed fusion additive manufacturing, Corros. Sci. vol. 128 (2017) 140–153.

[20] M. Song, M. Wang, X. Lou, R. Rebak, G. Was, Radiation damage and irradiation-assisted stress corrosion cracking of additively manufactured 316L stainless steels, J. Nucl. Mater. vol. 513 (2019) 33–44.

[21] A. Birnbaum, J. Steuben, E. Barrick, A. Iliopoulos, J. Michopoulos, Intrinsic strain aging, Σ3 boundaries, and origins of cellular substructure in additively manufactured 316L, Addit. Manuf. vol. 29 (100784) (2019), 100784.

[22] J. Trelewicz, G. Halada, O. Donaldson, G. Manogharan, Microstructure and corrosion resistance of laser additively manufactured 316L stainless steel, JOM vol. 850–859 (2016) 68–859.

[23] M. Laleh, A. Hughes, W. Xu, N. Haghdadi, K. Wang, P. Cizek, I. Gibson, M. Tan, On the unusual intergranular corrosion resistance of 316L stainless steel additively manufactured by selective laser melting, Corros. Sci. vol. 161 (108189) (2019), 108189.

[24] D. Kong, X. Ni, X. Dong, L. Zhang, C. Man, X. Cheng, X. Li, Anisotropy in the microstructure and mechanical property for the bulk and porous 316L stainless steel fabricated via selective laser melting, Mater. Lett. vol. 235 (2019) 1–5.

[25] O. Salman, C. Gammer, A. Chaubey, J. Eckert, S. Scudino, Effect of heat treatment on microstructure and mechanical properties of 316L steel synthesized by selective laser melting, Mater. Sci. Eng. A vol. 748 (2019) 205–212.

[26] A. Ettefagh, S. Guo, J. Raush, Corrosion performance of additively manufactured stainless steel parts: A review, Addit. Manuf. vol. 37 (101689) (2021).

[27] M. Laleh, A. Hughes, W. Xu, P. Cizek, M. Tan, Unanticipated drastic decline in pitting corrosion resistance of additively manufactured 316L stainless steel after high-temperature post-processing, Corros. Sci. vol. 165 (108412) (2020), 108412.

[28] K. Wang, Q. Chao, M. Annasamy, P. Hodgson, S. Thomas, N. Birbilis, D. Fabijanic, On the pitting behaviour of laser powder bed fusion prepared 316L stainless steel upon post-processing heat treatments, Corros. Sci. vol. 197 (110060) (2022), 110060.

[29] P. Dong, V. Vecchiato, Z. Yang, P. Hooper, M. Wenman, The effect of build direction and heat treatment on atmospheric stress corrosion cracking of laser powder bed fusion 316L austenitic stainless steel, Addit. Manuf. vol. 40 (101902) (2021), 101902.

[30] "Nuclear Grade Stainless Steel Procurement, Manufacturing, and Fabrication Guidelines," Electric Power Research Institute, Document #84-MG-18, Palo Alto, California, 1985.

[31] M. Bojinov, E. Jäppinen, T. Saario, K. Sipilä, A. Toivonen, Effect of lead and applied potential on corrosion of carbon steel in steam generator crevice solutions, Corros. Sci. vol. 159 (2019) 108–117.

[32] I. Betova, M. Bojinov, T. Ikäläinen, T. Saario, K. Sipilä, Corrosion of alloy 690 in simulated steam generator crevices – effect of applied potential, pH and Pb addition, J. Electrochem. Soc. vol. 169 (021502) (2022), 021502.

[33] R. Fonda, D. Rowenhorst, C. Feng, The effects of post-processing in additively manufactured 316L stainless steels, Met. Mater. Trans. A vol. 51 (2020) 6560–6573.

[34] S. Gao, Z. Hu, M. Duchamp, P. Sankara Rama Krishnan, S. Tekumalla, X. Song, M. Seita, Recrystallization-based grain boundary engineering of 316L stainless steel produced via selective laser melting, Acta Mater. vol. 200 (2020) 366–377.

[35] K. Bertsch, G. Meric de Bellefon, B. Kuehl, D. Thoma, Origin of dislocation structures in an additively manufactured austenitic stainless steel 316L, Acta Mater. vol. 199 (2020) 19–33.

[36] Y. Wang, T. Voisin, J. McKeown, J. Ye, N. Calta, Z. Li, Additively manufactured hierarchical stainless steels with high strength and ductility, Nat. Mater. vol. 17 (2017).

[37] N. Chen, G. Ma, W. Zhu, A. Godfrey, Z. Shen, G. Wu, X. Huang, Enhancement of an additive-manufactured austenitic stainless steel by post-manufacture heat-treatment, Mater. Sci. Eng. A vol. 759 (2019) 65–69.

[38] H. Atkinson, S. Davies, Fundamental aspects of hot isostatic pressing: an overview, Metall. Mater. Trans. A vol. 31 (2000) 2981–3000.

[39] C. Zhou, S. Hu, Q. Shi, H. Tao, Y. Song, J. Zheng, P. Xu, L. Zhang, Improvement of corrosion resistance of SS316L manufactured by selective laser melting through subcritical annealing, Corros. Sci. no. 108353 (2020), 108353.

[40] G. Sander, S. Thomas, V. Cruz, M. Jurg, N. Birbilis, X. Gao, M. Brameld, C. Hutchinson, On the corrosion and metastable pitting characteristics of 316L stainless steel produced by selective laser melting, Electrochem. Soc. Interface vol. 164 (2017) C250–C257.

[41] Q. Chao, V. Cruz, S. Thomas, On the enhanced corrosion resistance of a selective laser melted austenitic stainless steel, J. Scr. Mater. vol. 141 (2017) 94–98.

[42] R. Revilla, M. Calster, M. Raes, G. Arroud, F. Andreatta, L. Pyl, P. Guillaume, I. Graeve, Microstructure and corrosion behavior of 316L stainless steel prepared using different additive manufacturing methods: a comparative study bringing insights into the impact of microstructure on their passivity, Corros. Sci. vol. 176 (108914) (2020), 108914.

[43] R. Revilla, B. Wouters, F. Andreatta, A. Lanzutti, L. Fedrizzi, I. De Graeve, EIS comparative study and critical Equivalent Electrical Circuit (EEC) analysis of the native oxide layer of additive manufactured and wrought 316L stainless steel, Corros. Sci. vol. 167 (108480) (2020).

[44] M. Lodhi, K. Deen, M. Greenlee-Wacker, W. Haider, Additively manufactured 316L stainless steel with improved corrosion resistance and biological response for biomedical applications, Addit. Manuf. vol. 27 (2019) 8–19.

[45] C. Man, C. Dong, T. Liu, D. Kong, D. Wang, X. Li, The enhancement of microstructure on the passive and pitting behaviors of selective laser melting 316L SS in simulated body fluid, Appl. Surf. Sci. vol. 467–468 (2019) 193–205.

[46] A. Ettefagh, S. Guo, Electrochemical behavior of AISI316L stainless steel parts produced by laser-based powder bed fusion process and the effect of post annealing process, Addit. Manuf. vol. 22 (2018) 153–156.

[47] D. Kong, C. Dong, X. Ni, L. Zhang, J. Yao, C. Man, X. Cheng, K. Xiao, X. Li, Mechanical properties and corrosion behavior of selective lasermelted 316L stainless steel after different heat treatment processes, J. Mater. Sci. Technol. vol. 35 (2019) 1499–1507.

[48] R. Soulas, M. Cheynet, E. Rauch, T. Neisius, L. Legras, C. Domain, Y. Brechet, TEM investigations of the oxide layers formed on a 316L alloy in simulated PWR environment, J. Mater. Sci. vol. 48 (2013) 2861–2871.

[49] G. Bertali, M. Burke, F. Scenini, N. Huin, The effect of temperature on the preferential intergranular oxidation susceptibility of alloy 600, Metall. Mater. Trans. A vol. 49A (2018) 1879–1894.

[50] M. Shimada, H. Kokawa, Z. Wang, Optimization of grain boundary character distribution for intergranular corrosion resistant 304 stainless steel by twin-induced grain boundary engineering, J. Acta Mater. vol. 50 (2002) 2331–2341.

[51] Z. Zhou, Y.Z.J. Liu, H. Pang, G. Zhu, Non-precious nickel-based catalysts for hydrogen oxidation reaction in alkaline electrolyte, Electrochem. Commun. vol. 121 (106871) (2020), 106871.

[52] W. Ni, T. Wang, F. Héroguel, A. Krammer, S. Lee, L. Yao, A. Schüler, J. Luterbacher, Y. Yan, X. Hu, An efficient nickel hydrogen oxidation catalyst for hydroxide exchange membrane fuel cells, Nat. Mater. 21 (2022) 804–810.